Nebraska Center for Biotechnology: Faculty and Staff Publications

Biotechnology, Center for

12-26-2022

Multipolymer microsphere delivery of SARS-CoV-2 antigens

Farah Shahjin

Milankumar Patel

Jatin Machhi

Jacob D. Cohen

Mohammad Ullah Nayan

See next page for additional authors

Authors

Farah Shahjin, Milankumar Patel, Jatin Machhi, Jacob D. Cohen, Mohammad Ullah Nayan, Pravin Yeapuri, Chen Zhang, Emiko Waight, Mahmudul Hasan, Mai Mohamed Abdelmoaty, Prasanta K. Dash, You Zhou, Irene Andreu, Howard E. Gendelman, and Bhavesh D. Kevadiya

Full length article

Multipolymer microsphere delivery of SARS-CoV-2 antigens

Farah Shahjin[a,1], Milankumar Patel[a,1], Jatin Machhi[a], Jacob D. Cohen[a],
Mohammad Ullah Nayan[a], Pravin Yeapuri[a], Chen Zhang[a], Emiko Waight[a],
Mahmudul Hasan[b], Mai Mohamed Abdelmoaty[a], Prasanta K. Dash[a], You Zhou[c],
Irene Andreu[d], Howard E. Gendelman[a,*], Bhavesh D. Kevadiya[a]

[a] *Department of Pharmacology and Experimental Neuroscience, University of Nebraska Medical Center, Omaha, NE 68198-5800, USA*
[b] *Department of Pharmaceutical Sciences, University of Nebraska Medical Center, Omaha, NE, USA*
[c] *Center for Biotechnology, University of Nebraska-Lincoln, Lincoln, NE, USA*
[d] *RI Consortium of Nanoscience and Nanotechnology and Department of Chemical Engineering University of Rhode Island, RI, USA*

ABSTRACT

Effective antigen delivery facilitates antiviral vaccine success defined by effective immune protective responses against viral exposures. To improve severe acute respiratory syndrome coronavirus-2 (SARS-CoV-2) antigen delivery, a controlled biodegradable, stable, biocompatible, and nontoxic polymeric microsphere system was developed for chemically inactivated viral proteins. SARS-CoV-2 proteins encapsulated in polymeric microspheres induced robust antiviral immunity. The viral antigen-loaded microsphere system can preclude the need for repeat administrations, highlighting its potential as an effective vaccine.

Statement of significance

Successful SARS-CoV-2 vaccines were developed and quickly approved by the US Food and Drug Administration (FDA). However, each of the vaccines requires boosting as new variants arise. We posit that injectable biodegradable polymers represent a means for the sustained release of emerging viral antigens. The approach offers a means to reduce immunization frequency by predicting viral genomic variability. This strategy could lead to longer-lasting antiviral protective immunity. The current proof-of-concept multipolymer study for SARS-CoV-2 achieve these metrics.

1. Introduction

Biodegradable, single polymer microspheres (MS) advance therapeutic and vaccine delivery [1–6]. They serve as single-dose formulation which mimic the repeated injections recorded by conventional vaccinations. The delivery system offers both antigen priming and boosting. Notably, single polymer MS, such as poly(D,L-lactic-co-glycolic acid) (PLGA) MS [7], can deliver and release encapsulated antigens in continuous or pulsatile manners [7]. MS formulations offers some appealing features like sustained or pulsatile slow-controlled antigen release (SCAR). These demonstrate

controllable bioerosion and biocompatibility [6]. MS formulations also offer advantages by generating sustained antimicrobial immune responses. Infections prevented by persistent antigen stimulation and by boosting induction of memory cells can be realized through MS formulations. These can serve in a facilitatory manner for delivery of multiple dosing regimens. Although not yet extensively studied, beneficial effects of MS formulations show broad potential applications. For example, SCAR formulations were deployed in HIV-1gp120 and influenza immunizations in development of long-lasting protective immunity. These preclude needs for repeated immunizations [8,9]. Other benefits are associated with controlled release delivery. These offer the ability to simultaneously deliver, antigens and adjuvants, to dendritic cell and other antigen-presenting cells (APCs) serving to secure antigens and adjuvants in mounting immune responses and protecting the antigens against degradation. This occurs prior to the antigen reaching

the APCs for functionalization of site-directed delivery. The result is a robust cell-mediated immune anti-microbial response [10–13]. For example, PLGA MS serve as antigen, peptide, and subunit vaccine carriers [3,4,11,14]. PLGA MS provide extended pulsatile antigen release [8] and improved APC delivery [6,15].

To achieve "optimal" antigen release reflective of a multi-dose vaccine, we developed a biodegradable 'multiple polymer' MS. The rationale for a multipolymer platform was to blend polymers with fast and slow bioerosion rates, conferring the advantage of early and late release of its payload from the degrading components. MS systems offer advantages of eliminating the need for repetitive dosing and improving patient compliance. The MS was loaded with a whole, intact, chemically inactivated severe acute respiratory syndrome coronavirus 2 (SARS-CoV-2) to provide sustained antigen release for prime-boost dosing within a single formulation. This multipolymer MS were then tested for its ability to mount any antiviral immune response including memory and humoral components produced against the SARS-CoV-2 spike protein. We posit that with the known viral genomic variabilities that have evolved in circulation over time, such strategies can serve as a platform to deliver antigen in its whole inactive form and offer a broader range of antigenic epitopes. This is in addition to its generation of long-lasting antiviral immunity.

While inactivated virus-based vaccines provide safe and effective protection against influenza, poliovirus, mumps, rubella, and other pathogens [16] little is known on whether MS formulations can load and release SARS-CoV-2 to elicit immune response of similar magnitude to that of the commercially available vaccines. Development of such a platform could serve as reliable vaccine candidates through improved whole or subunit antigen delivery while providing platforms for multiple antigen loadings to elicit long term immunity. Herein, we developed and characterized a multipolymer MS delivery platform by microscopic and spectroscopic assays. MS porosity provides a large surface for efficient loading and controlled antigen release [17]. Additionally, porous MS influences antigen cross-presentation efficiency initiating virus clearance through T-cell mediated immune responses [18]. Moreover, we provide evidence of successful antigen encapsulation then demonstrate its functional capacity by eliciting antiviral immune responses. For proof of concept, only cellular antiviral responses against SARS-CoV-2 were affirmed (Fig. 1).

2. Materials and methods

2.1. Reagents

All reagents were purchased from Sigma Aldrich, St. Louis, MO, USA, unless stated otherwise. The polymers used include polycaprolactone (PCL) [Cat#19561, Polysciences, Inc., Warrington, PA, USA], poly (lactic-co-glycolic acid) (PLGA) 75:25 [Cat#P1941], polylactic acid (PLLA) – PLLA [Cat#765112]. Other reagents include 2-methylpentane (2-MP) [Cat#M65807], dichloromethane (DCM) [Cat#270997], dimethylformamide (DMF) [Cat#227056], polyvinyl alcohol (PVA, average 30,000–70,000 molecular weight) [Cat#P8136].

2.2. Whole, inactive SARS-CoV-2 antigen preparation and characterization

#### 2.2.1. SARS-CoV-2 propagation and inactivation

These SARS-CoV-2 related experiments were performed in the University of Nebraska Medical Center (UNMC) biosafety level 3 (BSL-3) core facility and approved by UNMC Institutional Biosafety Committee (IBC). The SARS-CoV-2 strain used in the study was the isolate USA-WI1/2020 (BEI, NR-52384). The virus was passaged on Vero E6 cells (ATCC (clone E6, ATCC, #CRL-1586) and maintained

in Eagle's minimal essential medium (EMEM, Gibco) supplemented with 10% fetal bovine serum, 100 units/ mL penicillin and streptomycin, 1% v/v MEM non-essential amino acids, and 1 mM sodium pyruvate at 37°C in a humidified CO_2 incubator. Viral stocks were produced by infecting Vero E6 cells at a multiplicity of infection (MOI) of 0.01 with viral recovery from infected cells after 96 h. The collected virus-infected culture supernatant was cleared by centrifugation at 5000 rpm and stored in aliquots at -80°C. Viral titer was determined using standard plaque assays [19]. For inactivation of the virus, 0.05% beta-propiolactone treatment was administered for 16 h at 4°C followed by 2 h at 37°C to hydrolyze residual beta-propiolactone. Following viral inactivation, assays that confirmed complete viral inactivation conducted including the evaluation of cytopathic effects (CPE) (Fig. S1a), immunostaining followed by confocal microscopy (Fig. S1b), standard plaque assay (Fig. S1c), and quantitative polymerase chain reaction (Fig. S1d). For qualitative determination of viral replication, Vero E6 cells were treated with active and inactive SARS-CoV-2 (MOI = 0.01) and incubated at 37°C in a 5% CO_2 incubator. The cells were monitored daily for 5 days for the presence of virus-induced CPE. Cell culture supernatants, collected before and 16 h after infection, were in parallel subjected to qPCR to determine the SARS-CoV-2 gene expression [20]. For immunostaining, Vero E6 cells were treated with active and inactive SARS-CoV-2 (MOI = 0.01) for 24 h. The following published protocol [21] using the antibodies against spike RBD (Cat#MAB105401) and spike S1 subunit (Cat#MAB105403) of SARS-CoV-2 was followed.

To confirm viral structural integrity, western blot tests [20], negative stain transmission electron microscopy (TEM), and atomic force microscopy (AFM) were performed. For western blotting, published protocol [20] using the antibodies against the spike S1 subunit (Cat#MAB105403, R&D Systems) and Nucleocapsid (MAB10474, R&D Systems) of SARS-CoV-2 was followed. For TEM, a 3 μl aliquot of the purified and concentrated sample was applied to a glow-discharged 400 mesh ultra-thin carbon grid (Electron Microscopy Sciences, G400NI) and stained with 2% uranyl formate. The grid is subsequently blotted dry by a piece of filter paper. The TEM grid is imaged in an FEI Tecnai 300kV Field emission gun TEM (Thermo Fisher Scientific) on a Gatan Summit K2 direct electron detector camera (Gatan Inc., Pleasanton, CA). For AFM imaging and image analysis, freshly cleaved mica was modified with 1-(3-aminopropyl)-silatrane (APS) as previously described [22,23]. Samples were diluted in PBS buffer and deposited onto the piece of APS mica. After a 2 min incubation samples were rinsed briefly with several drops of deionized water and dried with a gentle flow of argon. Images were collected with the MultiMode Nanoscope IV system (Bruker Instruments, Santa Barbara, CA) in Tapping Mode at ambient conditions. Silicon probes RTESPA-300 (Bruker Nano Inc., CA, USA) with a resonance frequency of ~300 kHz and a spring constant of ~40 N/m were used for imaging at a scanning rate of about 1 Hz. Images were processed using the FemtoScan software package (Advanced Technologies Center, Moscow, Russia).

2.2.2. Preparation of porous multipolymer MS

PCL (100 mg), PLGA 75:25 (100 mg), and PLLA (50 mg) was dissolved in 1 mL of DCM. Porogen (300 uL of 2-methylpentane) was mixed and vortexed with 3 mL of DMF. The organic phase was added to the aqueous phase, consisting of 1% (w/v) 200-300 mL polyvinyl alcohol in a 600 mL capacity glass beaker (8.2 cm diameter) with constant stirring using a pitched blade propellor (Cat#14-500-363, Fisherbrand, Denver, CO, USA), at 1000 rpm with an overhead stirrer (3593001, IKA, Wilmington, NC, USA). The solution was left stirring overnight for organic solvent evaporation and polymer phase inversion. The porous multipolymer MS were collected either by filtration of aqueous phase using Whatman filter paper (#1). Milli-Q water washes (~500 mL) were done to re-
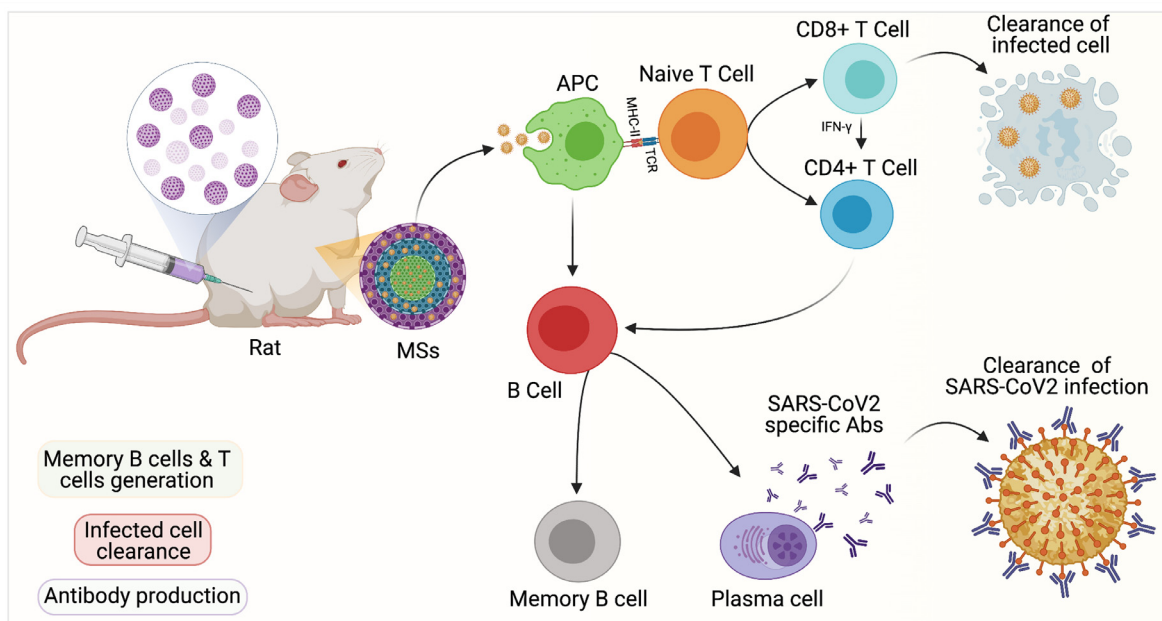
Fig. 1. Proposed protective antiviral immune responses from MS-based SARS-CoV-2 antigen delivery. Following intramuscular injection of the MS (porous spheres) loaded with whole, inactive SARS-CoV-2 (yellow spheres) in different layers, antigen release and delivery to antigen presenting cells (APC) is anticipated to generate humoral (B-cell generation and antibody production by plasma cells) and cellular (T-cell activation, cytokine release by CD4 and CD8 T-cell subsets) responses. This leads to protective antiviral immunity. The antibodies generated by the plasma cells and the activated T-cell subsets, both aid in clearance of infection.

move PVA. MS were lyophilized to powder form. In case of antigen loading, the above solvent evaporation method was repeated with minor changes. To maintain MS sterility, solvent evaporation was performed under the cell culture hood. Total viral protein (25 mg as determined by bicinchoninic acid assay) was added to 1 % PVA, stirred in the beaker at 300 rpm for 5 min, prior to adding the organic-polymer phase.

2.3. Microscopic characterization of multipolymer MS architecture

2.3.1. Scanning electron microscopy (SEM)

Lyophilized MS were collected on conductive adhesive carbon tape and attached to aluminum stubs. Particles were sputter-coated (Hummer VI Sputter Coater, Anatech) with ∼ 50 nm gold-palladium (10 mA for 5 minutes) and imaged at 5-12.5 kV on an FEI Quanta 200 operating in high vacuum mode. For the temperature stability study, MS (200 mg) was stored at room temperature, 4°C, -20°C and -80°C. At different time points, samples were collected for SEM. For the cellular interaction study, MS treated monocyte-derived macrophages (MDMs) were fixed by immersion in a solution of 2% glutaraldehyde, and 2% paraformaldehyde in a 0.1M Sorenson's phosphate buffer (pH 6.2) for a minimum of 24 h at 4°C. Samples were then washed three times, 10 minutes each, with phosphate buffer to clear excess fixative. They were post-fixed in a 1% aqueous solution of osmium tetroxide for 30 min to aid in conductivity. Samples were then washed again in phosphate buffer three times for 10 minutes each. Subsequently, samples were dehydrated in a graded ethanol series (50, 70, 90, 95, 100, 100, 100%). After dehydration, samples were washed three times in hexamethyldisilazane and allowed to air-dry overnight. The samples were then attached to aluminum SEM stubs with double-sided carbon tape. The following day, the samples were sputter-coated and imaged as mentioned above. For cross-sectioning of the MS prior to SEM, we developed a cost-effective bench method for a quick technique to section MS. Briefly, MS was immobilized in a gel matrix (commercial beauty product, Hemp⁺ facemask by My Beauty Spot, Amazon, USA) in a suitable mold (e.g., ultracentrifuge tubes,

that can be cut by the blade). The MS-gel matrix was frozen at -80°C for 5 minutes and 5-10 μm sections were obtained using Leica CM1850 (Leica Biosystems Inc, IL, USA) set at -20°C. The slices were collected in warm water to wash off the water-soluble gel matrix and centrifuged at 1000 rpm to pellet the MS sections. Water washes were repeated. To study the effect of temperature on the MS morphology, MS (200 mg) was stored at room temperature, 4°C, -20°C and -80°C. At different time points, samples were collected for SEM.

MS porosity was measured using Fiji [24] from a cropped SEM image representing a planar particle surface. First, the scale of the image was set from the original SEM scale bar. Next, a Gaussian blur was applied. The images were then transformed using a Bandpass filter. This excluded large structures down to 40 pixels and small structures up to 3 pixels with a 5% tolerance level. The image thresholding was performed using the Otsu's method [25] to distinguish the pores from the surface. Finally, particle plug-in was used to recognize the pores and its sizes.

2.3.2. X-ray microscopy (XRM)

Dry powder of MS was run on a Zeiss Xradia Versa 610 X-ray microscope operated at 80 kV, 10 kW, 4X optical magnification at 1.54 μm voxel size with 1s exposure time and 2401 projections, to achieve a 3D reconstruction of the sample. The obtained tomograms were analyzed with Dragonfly Pro (Object Research Systems, version 2021.1.0.977) to calculate particle size and porosity. The tomograms were filtered using a Gaussian blur to remove low-frequency noise. Then the tomograms were segmented into polymer and void space using the Dragonfly Pro machine learning module. The segmented particles were separated using watershed and their minimum Feret diameters were calculated to obtain the size distribution. Fibrous debris or particles not completely captured or separated in the tomogram were excluded in the size distribution. To calculate the porosity, the polymer particle pores were virtually filled to obtain the volume of the solid spheres. The porosity was expressed as volume of pores / total sphere volume in units of %.

2.4. Spectroscopic and thermal characterizations

2.4.1. Confocal Raman microscopy

Selected MS were sectioned by freezing a droplet of MS suspension in water using liquid nitrogen and sectioning the frozen droplet using a steel razor blade. The MS were air dried on a glass slide and imaged on a WITec alpha 300R confocal Raman microscope equipped with a 532 nm laser and a 600 g/mm grating. Raman hyperspectral maps were obtained using a 50x objective (Zeiss Epiplan-NEOFLUAR NA=0.8), a laser power of 5 mW and 10 accumulations of 1s per data point, with 20 μm between data points. The hyperspectral maps were processed by TrueComponent™ on the WITec Project Five software to find the two main components of the mapped region. Single spectra of pure PCL, PLGA and PLLA were acquired on the same system and compared to the components found on the multipolymer MS.

2.4.2. Fourier transform infrared spectroscopy (FTIR)

FTIR were recorded on a Perkin-Elmer-spectrum attenuated total reflectance (ATR)-FTIR equipped with a UATR-accessory (Perkinelmer, Inc., Waltham, MA, USA) [26]. The spectra were recorded for the individual and multipolymer MS. The scanning range was 400-4000 cm^{-1}, and the resolution was 2 cm^{-1}.

2.4.3. X-ray photoelectron spectroscopy (XPS)

XPS measurements were carried out using monochromatic Al K_a X-ray with an energy of 1486.6 eV by the K-alpha XPS system (ThermoFisher Scientific, Waltham, MA, USA) [27]. The spectra were generated using GraphPad Prism 9.2 software.

2.4.4. X-ray powder diffraction (XRD)

The crystalline nature of the MS was investigated using Rigaku SmartLab Diffractometer (Rigaku Corporation, Tokyo, Japan), operated with Cu Kα radiation at 40 kV and 30 mA [27]. A length limiting slit of 10 mm, a divergence slit of 1/2 degree and a 5° Soller slit were used on the incident beam path and the data was collected by q/2q scans using a D/tex Ultra 250 1D strip detector with 20 mm receiving slits and a 5-degree Soller slit. A Ni foil was used to suppress Kb intensity. The samples were spread in a 20 × 20 mm, 0.2 mm deep pocket of the sample holder and the surface was leveled. The data was collected from 15 to 35 degrees, continuously scanning q/2q scan at 0.6s/step with a step size of 0.01. The spectra were generated using OriginPro 2021 software.

2.4.5. Thermogravimetric analysis (TGA)

The thermal properties of the samples were measured using NETZSCH TGA 209 F1 Libra system (NETZSCH, Waldkraiburg, Bayern, Germany). TGA thermograms were obtained between 20 and 700°C with a constant heating rate of 10°C/min under nitrogen gas (flow rate of 20 ml/min). This was completed using an alumina (Al_2O_3) crucible containing about 17 mg of sample. The data was analyzed using NETZSCH Proteus-thermal analysis-Version 6.1.0 software. The spectra were generated using OriginPro 2021 software.

2.5. Human monocyte-derived macrophage (MDM) cell cultures

Human monocytes were isolated by leukapheresis from HIV-1/2 and hepatitis seronegative donors according to an approved UNMC IRB exempt protocol. Human monocytes were plated in 6 well plates at a density of 1.5 × 10^6 cells per well and on coverslips in 12 well plates at a density of 1.0 × 10^6 cells per well, using DMEM supplemented with 10% heat-inactivated pooled human serum, 1% glutamine, 10 μg/mL ciprofloxacin, and 50 μg/mL gentamicin. Cells were incubated at 37°C in a 5% CO_2 incubator.

After 7 days of differentiation in the presence of 1000 U/mL recombinant human macrophage colony stimulating factor (MCSF). MDMs were treated with 5 mg of MS. At day 7 of the treatment, MS-cell interactions were visualized by light microscopy (in 6 well plates), taken using a Nikon TE300 microscope (Nikon Instrument, Inc., Melville, NY, USA) at 20x objective for treated and untreated cells. In parallel, SEM (in 12 well plate) and TEM evaluations were performed [28].

2.6. Confocal laser scanning microscopy

For CLSM to detect SARS-CoV-2 loading in MS, the antigen loaded MS were fixed in 4% paraformaldehyde for 1.5 h, rinsed with 1x PBS twice, and incubated in 1x PBS containing 200 nM DAPI at 4 °C for 30 min. The samples were then mounted onto a glass slide using Fluor-G mounting medium and coverslip. Allowing 1 h air polymerization of the mounting medium in dark at room temperature, the slides with the stained virus and particles were examined under a Nikon A1r on a Ti2 inverted confocal laser scanning imaging system (Nikon Instruments Inc., Melville, NY, USA). A series of optical sections (0.5-1 um each Z-step) were collected using dual excitation and dual emission mode (405 nm laser for DAPI, 561 nm laser for polymer autofluorescence; 425 nm and 590 nm emissions respectively). The green color was used for DAPI signals for better visualization with red color autofluorescence. Overlaid images and 3D reconstruction movies from the series of Z-optical scan were obtained using Nikon NIS Element advanced image analysis program.

2.7. Animal studies

All animal studies were approved by the University of Nebraska Medical Center Institutional Animal Care and Use Committee in accordance with standards from the Guide for the Care and Use of Laboratory Animals (National Research Council of the National Academies, 2011). Male and female Sprague Dawley rats (∼ 270 g; Jackson Labs, Bar Harbor, ME) were maintained on a normal diet and water. Animal weights were monitored at the start and end of the study. For the treatment group, the rats were administered a single dose of 6 μg/g of body weight of chemically inactivated SARS-CoV-2 loaded MS. Injection was given intramuscularly (IM) into the caudal thigh muscle to determine the humoral and cellular immune response over 4 weeks. Control groups had rats treated with either vehicle only or MS without inactive SARS-CoV-2 antigen. On days 7 and 28, rats were terminally anesthetized with isoflurane, and blood was collected by cardiac puncture in K_3EDTA tubes for flow cytometry and heparin tubes for plasma-based humoral tests. Spleen collected from the rats were isolated in RPMI media, immediately processed for flow cytometric analysis or frozen at -80°C for future use.

2.8. ELISA for humoral antiviral responses

Evaluation of SARS-CoV-2 Nucleoprotein (N) and Spike-Receptor Binding Domain (S-RBD) IgGs were performed by ELISA using titration ELISA assay kits. For these assays rat, SARS-CoV-2 IgG to Spike RBD Protein (SKU: KBVH015-22, Eagle Biosciences, Amherst ritu NH, USA) and Rat Anti-SARS-CoV-2 IgG to N (SKU: KBVH015-23, Eagle Biosciences) were applied according to the manufacturer's instructions. The plasma samples were diluted 100 x for the assays.

2.9. Flow cytometry

Samples were prepared for extracellular and intracellular cytokine staining in response to MS-Ag treatments. For extracellular staining, 2 × 10^6 of spleen cells were first stained with

LIVE/DEAD[TM] Fixable Blue Dead Cell Stain Kit in PBS for 30 min. After saline washes, cells were then stained with CD3-PE (201412, Biolegend), CD4-BUV737 (741770, BD Biosciences), CD8a-BV650 (740514, BD Biosciences), CD62L-eFluor660 (50-0623-82), CD44-APC Cy7 (NB600-1317APCCY7, Novus Biologicals), CD69-AlexaFluor488 (bs-2499R-A488) antibodies to detect surface antigens. For intracellular staining, 2×10^6 spleen cells, were plated in 12 well plates and stimulated with interleukin (IL-2, 1 µg/ mL, 200-02-250UG, Peprotech) for 5 hours, followed by stimulation with S-peptide (RP30020, Genscript) and Brefeldin A (4506521, eBioscience) for 12h. Cells were stained with LIVE/DEAD[TM] Fixable Blue Dead Cell Stain Kit in PBS, for 30 min and washed, then stained for surface markers with CD3 PE and CD4-BUV737 antibodies for 30 min at room temperature. Cells were then permeabilized using a transcription factor staining buffer kit (552300, eBioscience) for 45 min at 4°C followed by incubation with IFNγ-AlexaFluor488 (bs-0480R-A488, Bioss Antibodies), IL-4-(OX81) eFluor660 (50-7045-82, Thermofisher Scientific), and IL17RB-Alexa Fluor 680 (bs-2610R-A680, Bioss Antibodies) antibodies for 30 min at 4°C. All stained cells were fixed in 1% formaldehyde. Isotype and fluorescence-minus-one (FMO) control used for each of the antibodies. This enabled accurate gating during flow cytometric analyses for each of the cell subsets. Whole blood, 60 µl of blood was stained for flow cytometric analysis in replicate tests. All flow cytometry data was acquired on a BD LSR II flow cytometer and analyzed using BD FACSDiva[TM] Software v8 (BD Biosciences, San Jose, CA, USA). Untreated and single stained controls were used to assign gates for each fluorophore.

2.10. Toxicity profiling

Serum chemistry profile, complete blood counts (CBCs), and histological evaluations were used to assess systemic reactions to the MSMS carried antigens administered to the rats. At days 7 and 28, 100 µL blood was collected into K_2EDTA collection tubes for CBC tests or into heparinized blood collection tubes for blood chemistry and metabolite levels. Metabolic panels were completed using VetScan Chemistry Comprehensive Diagnostic Profile reagent rotor (Abaxis) on a VetScan VS2 machine [28]. For CBC tests whole blood collected from K_2EDTA tubes was assayed on a VetScan HM5 machine [26]. For both, the results for treated rats were compared with those from age- and sex-matched untreated controls. Histological examination was performed on 5 µm tissue sections stained with hematoxylin and eosin staining [28]. The images were captured on a Nuance EX multispectral imaging system affixed to a Nikon Eclipse E800 microscope (Nikon Instruments) and evaluated.

2.11. Statistics

Data were analyzed with GraphPad Prism 9.2 (GraphPad, La Jolla, CA, USA) and OriginPro software. Unless specified, data are presented as mean±SEM in all experiments. For flow cytometry, the statistical significance was assessed by One-way ANOVA followed by Newman/Keul's post-hoc analysis for multiple comparisons. Experiments with multiple time points were analyzed using Two-way ANOVA and Tukey's post-hoc tests for multiple comparisons. ($*P < 0.05$; $**P < 0.01$; $***P < 0.001$; $****P < 0.0001$; n.s., not significant).

3. Results

3.1. Antigen loaded porous multipolymer MS

Purified inactivated virus have been traditionally used for vaccine development. Such vaccine platforms are found to be safe and effective for the prevention of viral diseases such as influenza and polio viruses [29,30]. To develop and test a biodegradable polymer-based vaccine platform we produced inactivated SARS-CoV-2 and loaded it into a porous multipolymer MS [20,31].

We assured viral antigen integrity post inactivation by molecular and microscopic analyses. The topography (height and diameter) of the inactive virus was determined to compare that of the native, infectious virus. Based on the topographical images (Fig. 2a), the dimensions of the inactive virus, diameter was 106 ± 26.5 nm ($n = 89$) (Fig. 2b) with a topographical maximal central height of 25.9 ± 3.7 nm ($n = 89$) (Fig. 2c) comparable to the intact infectious virus examined by atomic force microscopy (AFM) [32,33]. To affirm the AFM topographical measurements, transmission electron microscopy (TEM) was performed for visualizations (Fig. 2d). The TEM results were consistent with the AFM measurements. Biochemical characterization served to ensure that the viral immunogenic epitopes were intact. This characterization included the viral spike (S) and nucleoproteins (N) present on the surface envelope and ribonucleoprotein core, respectively [34,35].

Western blot tests ensured the presence of both S and N viral proteins in the inactivated SARS-CoV-2 stocks. These tests (Fig. 2e) showed two intense bands, at 50 kDa for the N and 90 kDa for S proteins [36]. The data confirmed that inactivation did not alter the major epitopes required for eliciting antiviral immune responses.

Single emulsion solvent evaporation method was used to prepare multipolymer MS, composed of PCL, PLGA and PLLA.

Scanning electron microscopic images (SEM) shown in Fig. 3a, b demonstrated the non-porous multipolymer MS, compared to the porous MS, which was successfully generated using 2-methylpentane (2-MP). Owing to the blend of the polymers, the porogen conferred various pore sizes and surface depth to the MS surface. The porogen generated larger pores in PLLA compared to PLGA. Therefore, PLLA was used and admixed to generate larger and deeper pores (Fig. S2). Known differences in release kinetics between porous and non-porous MS [37–39] were supported by SEM morphological analyses. These demonstrated polymer separation and distribution (Fig. 3c, yellow and red arrows); whereas the external morphology was captured by X-ray microscopy (Fig. S3).

Solvent evaporation was performed for inactive SARS-CoV-2 loaded MS production. SEM images (Fig. 3d) showed no changes in antigen-loaded MS's external morphology. The particles showed the same porous patterns without a payload. Prior to functional investigations, the microscopic data of the MS (without antigen) was corroborated then detailed using state-of-art spectroscopic methods. Viral loading was confirmed by confocal laser scanning microscopic (CLSM) examination.

3.2. Advanced MS microscopic and spectral characterizations

3.2.1. Raman confocal-spectroscopy and X-ray microscopy (XRM)

To verify the composition of MS, microscopy and spectral analyses were performed. Raman hyperspectral mapping and optical microscopy (Fig. 4a,b) supported the observed SEM images demonstrating distinct separation and distribution of the polymers. Confocal Raman microscopy with spectral data (Fig. 4c,d) demonstrated spatial filtering depicting the external (cyan) and internal (magenta) dimensions corresponding to the presence of the PLGA and PCL components. Characteristic peaks belonging to PCL [2916, 2871, 1729, 1444, 1307, 1111, and 1051 cm^{-1}], PLGA 75:25 - [3006, 2951, 2884, 1769, and 1459 cm^{-1}], and PLLA - [3004, 2949, 2886, 1770, and 1460 cm^{-1} were identified in the spectra. The characteristic peaks of the raw polymers were seen to overlap with distinct peaks obtained from the blend from the PLGA/PLLA/PCL MS. Characteristic peaks of neat PCL overlap, in measure, with the spectra of the internal patch of polymer at 2922, 2873, 1731, 1449, 1310, 1113 and 1057 cm^1. Characteristic peaks of PLGA nearly overlap with the spectra of the external thin layer of the polymer at
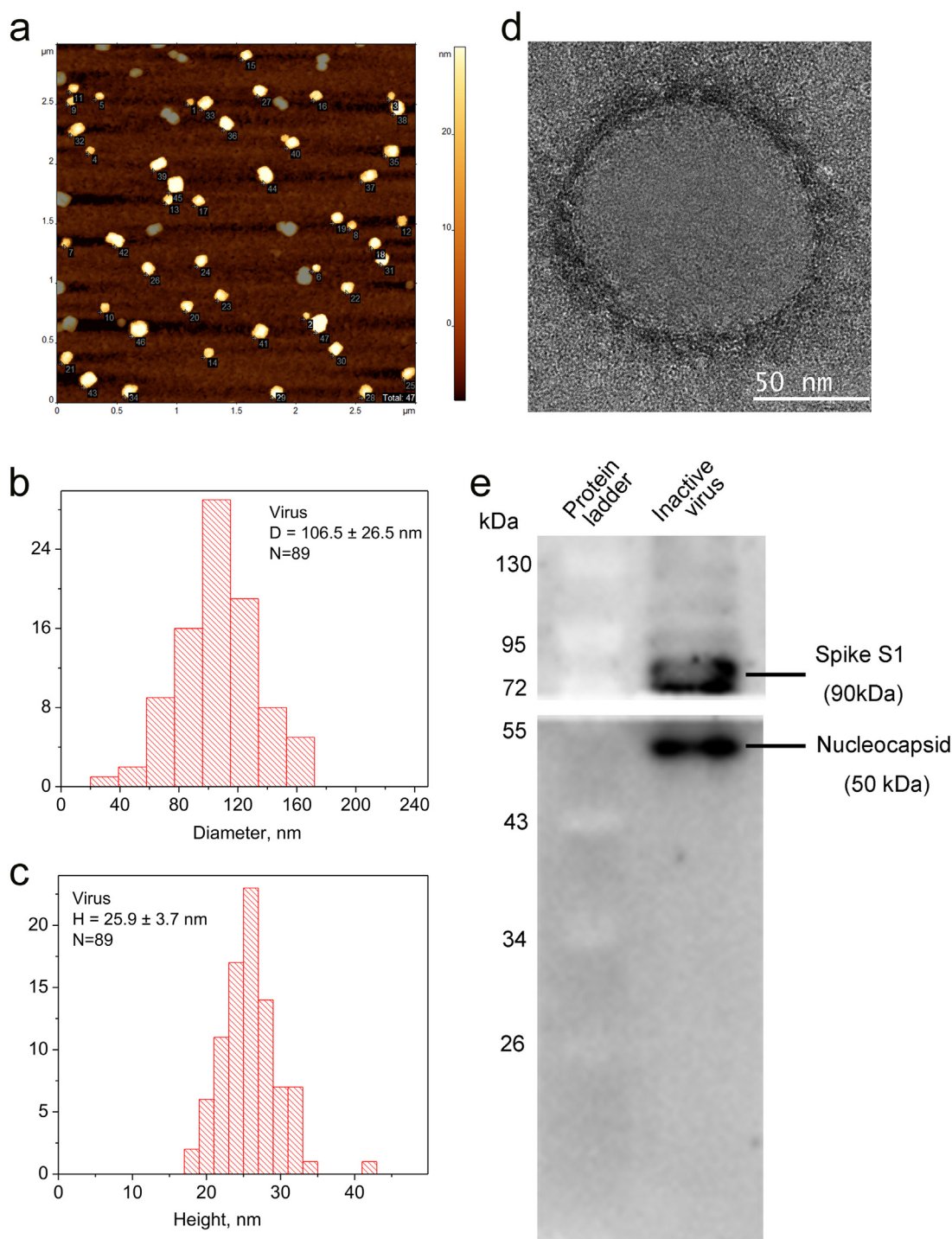
Fig. 2. Characterization of an "putative" inactive SARS-CoV-2 vaccine. (a) Topographic images of inactive SARS-CoV-2 was acquired by adsorbing the virions on APS modified mica and subsequent AFM image analysis. Topographical maximal (b) diameter was 25.9 ± 3.7 nm and (c) central height was 106 ± 26.5 nm (n = 89). (d) Representative negative stain TEM image of an inactive SARS-CoV-2 virion taken under magnification of 39000x, and (e) western blot analysis of SARS-CoV-2 Spike S1 (90 kDA) and Nucleocapsid (50 kDA) proteins of inactive SARS-CoV-2.

3008, 2951, 2884, 1774, and 1462 cm^{-1}. PLLA peaks overlap with the spectra of the shell and core, but not PCL at 3004, 2949, and 1770 cm^{-1}. These results indicated that the PLLA was incorporated into both the shell and core. The Raman spectra of PLLA and PLGA were indistinguishable due to the similarities in molecular polymer structures. While the absolute distinct layers of polymers were not visualized, the fast-degrading PLGA comprised the external thin matrix and the slow degrading PCL comprised the internal matrix. There was an indistinct distribution of the PLLA. These results align with the SEM observations where the polymer distribution proved inconsistent.

XRM was used to obtain MicroCT 3D reconstruction of the MS (Fig. 4e) showed a highly porous structure, with 37 % porosity. The histogram of the 3D particles' diameters obtained from
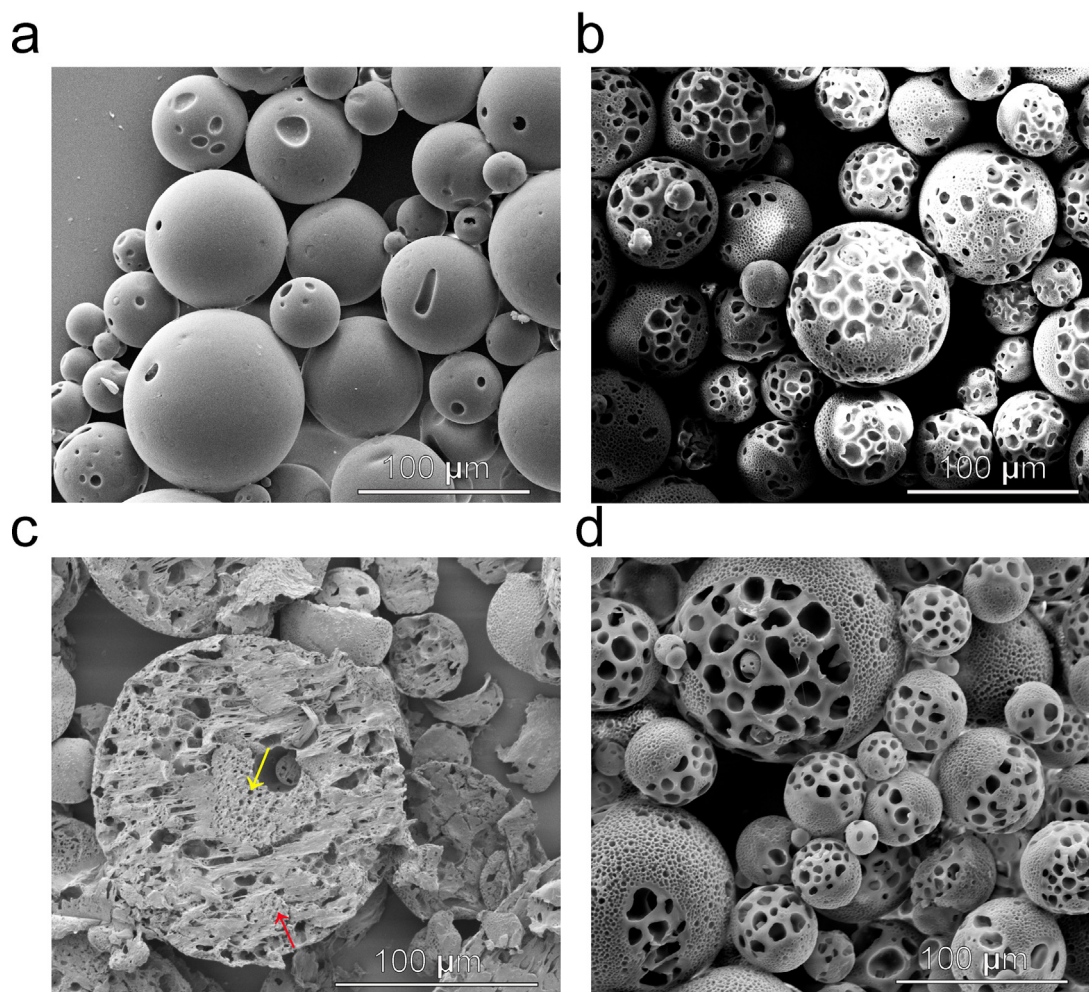
Fig. 3. Morphological depiction of the multipolymer MS. SEM images show external morphology of (a) non-porous MS, and (b) porous MS. (c) Cross section of porous MS showing the polymer distribution into distinct 'patches' as indicated by yellow and red arrows. (d) external morphology of porous MS with antigen (whole inactive SARS-CoV-2 virus). Scale bar: depicted at the lower bar of respective images.

XRM ($n = 5102$) showed that the MS diameters ranged from 15 to 143 μm, with an average particle size of 51 μm $\pm$ 17.5 μm (Fig. 4f).

3.2.2. Fourier transform infrared spectroscopy (FTIR)

To corroborate the Raman spectral results, Fourier-transform infrared spectroscopy (FTIR) was employed. It was used to verify the functional groups of the polymers existing within the samples (Fig. S4a). FTIR spectrum of the individual polymers – PCL, PLGA, PLLA and the MS are shown in Fig. S4a. In the case of raw PLGA 75:25, the IR peaks at 2994 and 2943 cm^{-1} correspond to the C-H stretch of -CH$_2$, and the C-H stretch of -CH respectively, 1748 cm^{-1} was assigned to the stretching vibration of the carbonyl group (C=O) of the ester bond, and 1083 cm^{-1} was attributed to C-O stretching. For the raw PCL, bands were at 2943-2864 cm^{-1} (CH$_2$ stretch) and 1045–1165 cm^{-1} (C-O stretch). Also, characteristic IR peaks were obtained at 1722 cm^1, corresponding to the conjugated carbonyl group (C=O). These were present in the region of 1000 to 1500 cm^{-1} and corresponded to C-C, C-H, and C-O groups. Like PLGA, PLLA also showed bands in the region 2997 and 2946 for C-H stretching. Bands 1755 and 1085 cm^{-1} were due to the stretch of the C=O and C-O groups, respectively. These experimental spectra match with the individual polymers [39–41]. All the absorption bands that the MS presented, at 2955, 2871, 1750, and 1084 cm^{-1}

closely superimposed with those of the individual polymers, confirming the triple polymer MS composition.

3.2.3. X-ray photoelectron spectroscopy (XPS)

Surface element analysis was performed by XPS to obtain qualitative (peak position indicating the elemental quantity) determinations of the functional groups present on the MS shell [42,43]. The observed survey spectrum indicated that the -C and -O were the predominant elements on the surface of the multipolymer MS as well as for the individual polymers (Fig. S5a). Binding energies of 285 and 532 eV were attributed to the C1s and O1s, respectively. The high-energy resolution C1s spectrum (Fig. S5b) showed the presence or absence of the chemical states of carbon, in approximate order of increasing binding energies, at ~285 eV, ~287 eV, ~289 eV, corresponding to functional groups C-C/C-H, C-O, and O=C-O, respectively. The values were in accordance with the binding energy values found in the literature for the respective polymers [44–46]. The XPS spectra for MS had similar peaks and valleys as that of PLGA and PCL, at ~285.0 and ~289.0 eV, where the latter peak was exactly superimposed with PLGA spectra for the O=C-O group. However, an increase in peak intensities at ~285.0 eV was observed, possibly due to the (i) admixture of multiple polymers that affected the surface chemical composition and charge, and (ii) presence of pores that increased the surface area
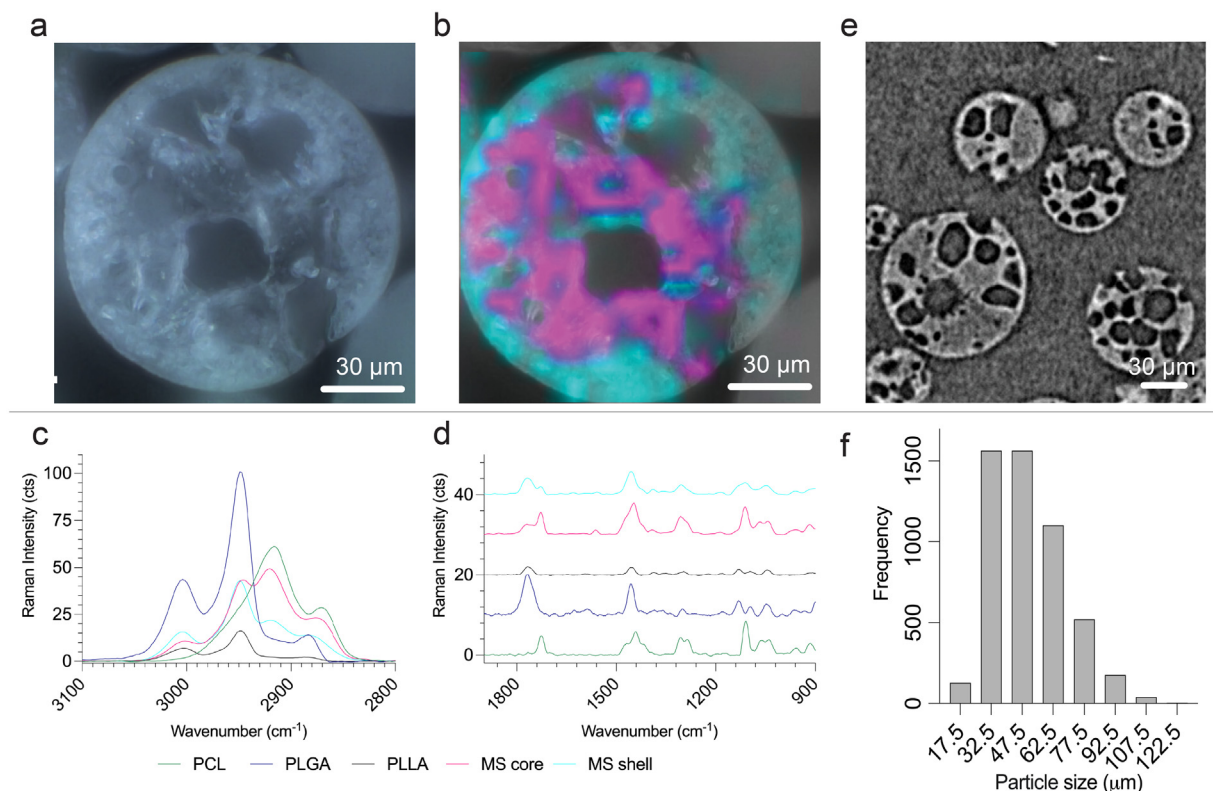
Fig. 4. Spectroscopic characterization of the multipolymer MS. (a) Brightfield microscopy image of a representative sectioned multipolymer MS, and (b) overlaid spatial distribution of the component polymers generated by Raman spectroscopy, showing the 'patchy' polymer distribution with PCL (magenta) and PLGA (cyan) as the internal and external polymer matrices, respectively, (c-d) Comparison of the Raman spectra from the internal (magenta) and external (cyan) regions of the multipolymer MS and the individual polymers –PCL (green), PLGA (blue) and PLLA (black) within the range of 900 to 3100 wavenumber (cm^{-1}), (e) A representative virtual cross section of a few MS as measured by X-ray tomography showing porous morphology, and (f) a histogram of the 3D particle diameter was obtained from X-ray tomography ($n = 5102$).

for electron emission. Moreover, past studies have demonstrated that surface geometry significantly influences spectral intensities of photoelectron measures at different emission angles [47–50]. As shown by the XRM data above, the pores extend throughout the particle.

This possibly explains the XPS reading of the surface elemental composition for the MS reflecting the presence of both PCL and PLGA at the same time. The high-energy resolution O1s spectrum (Fig. S5c) showed the binding energy peak at ∼532 eV corresponding to the functional group O=C [51]. The decrease in the binding energy of MS compared to raw polymers may be attributed to the surface charges that affect the emitted electron' kinetic energy during scan. Overall, the MS generated were composed of a 'patchy' distribution of the selected polymers, with the MS' surface elemental distribution corresponded PCL, PLGA, and PLLA.

3.2.4. X-ray diffraction spectroscopy (XRD)

The XPS data was further corroborated using X-Ray diffraction (XRD) analyses to identify the MS bulk composition. Three peaks in the XRD were obtained at diffraction angles of 2 θ; ∼21°, ∼22.0°, and ∼23.5°, indicating that raw PCL and MS were in its semi-crystalline form (Fig. S4b). On the other hand, raw PLGA and PLLA had no distinct peaks, indicating it remained in the amorphous form. In theory, XRD identifies crystalline materials within about 10 μm and owing to the design of the MS where surface of the particles was composed of giant pores, the XRD curve revealed the surface composition, which constituted PCL with the other polymers.

3.3. Thermal characterization of porous, layer-by-layer microspheres

3.3.1. Thermogravimetric analysis (TGA) and differential thermal analysis (DTA)

The thermal degradation properties were characterized using a TGA (Fig. S6a). The thermal degradation of the PLGA copolymer was like the PLLA homopolymer, occurring between 290 to 350°C (mass changes of 100 and 99.39 % respectively), and for PCL, between 400 to 440°C (mass change = 95.56 %). The thermal properties of the raw polymers were reflective of the previously published thermograms [52–54] The shift in the curve of MS, showed the degradation of the MS occurred at a lower temperature than PCL but at a higher temperature than PLGA/PLLA, which can be attributed to the admixture of PLGA and PLLA with PCL. The thermal stability of MS was plotted as DTA thermograms (Fig. S6b). PCL showed extreme weight reduction at 405°C, PLLA at 342°C, and PLGA between 330°C and 345°C. The thermogram for MS showed two distinct peaks, at 347°C and 415°C, corresponding to the decomposition peaks of the individual polymers, PLGA/PLLA and PCL respectively. The overall curve MS shift had a weight loss pattern and decompositions reflective of all three polymers. These affirmed the presence of PCL, PLGA and PLLA in the MS.

3.3.2. Storage temperature stability

In addition to examining the thermal stability of the MS, it is also important to identify the suitable long-term storage temperatures for these particles, if these particles are intended to be deployed as protein/peptide-based delivery systems. Long-term storage must preserve the cargo and protect the delivery systems. To

investigate the stability of the MS, a visual inspection was performed by SEM to investigate any changes in particle morphology across storage temperatures 4°C, -20°C, -80°C, as compared to room temperatures (RT) which are ideally used for parenteral formulations. SEM images were taken at 7, 28, 42, and 130 days (Fig. S6c). No visible particle degradation or changes in porosity patterns were observed, ensuring that carrier particles were stable at any of the selected temperatures. It was concluded from all the thermal analysis that our lyophilized MS can be stored at any of the usual temperatures ideal for drug/peptide storage and can endure high and low temperatures, without changes in polymer chemistry and particle morphology. The storage stability of microencapsulated antigens is expected to be improved over that of fluid formulations. Notably antigen stability is greater in a dry state than in solution [55,56].

3.4. Cellular interactions of MS with antigen-presenting cells

Regardless of the route of administration of the MS, the primary responding cells will have initial interactions with the MS engulfed into phagosomes. Literature suggests that particle sizes are crucial to determine the extent of engulfment and clearance of the polymer MS from the body [57]. The MS were designed to be within size ranges of ~15 to 120 μm and were, in the majority, less likely to be engulfed by the phagocytes. Regardless of whether phagocytosis is sought or avoided, understanding the MS interaction with phagocytes is important to predict the MS biodegradation process.

Therefore, we treated the monocyte-derived macrophages (MDM), a primary responding APC in biological systems, with MS and incubated for 7 days to observe the particle-macrophage interaction using microscopic techniques. Simple light microscopic observations revealed that the control (untreated) cells remained uniformly spread out on the culture dish (Fig. 5a), while the MS-treated cells that migrated towards and crowded around the MS overtime (Fig. 5b, blue arrows). Compared to control cells (Fig. 5c), TEM showed that the MS were taken up by the MDMs (Fig. 5d). Similarly, compared to control cells (Fig. 5e), SEM images showed that the MS treated MDMs were seen to cluster around the particles (Fig. 5f) and engulf the smaller particles (Fig. 5g-h, yellow arrows). Overall, the SEM and TEM images revealed that smaller MS could undergo phagocytic engulfment. This occurrence mandates consideration of cellular engulfment for testing and modeling of the MS biodegradation process.

3.5. Characterization of inactive SARS-CoV-2 loaded multipolymer MS

Confirmation of cargo loading within particles is investigated by release in the case of drug payloads [58,59] for quantitative high-performance liquid chromatography or fluorophore-tagged payload for visualization by CLSM [60,61]. High resolution image Z-axis optical acquisition with dual-excitation and dual-emission mode was used to identify viral loading into the porous MS was carried out using a Nikon A1r CLSM (Fig. 5i; images overlaid from surface 30 optical scans). The 3-D reconstructed images were obtained from series of Z-optical scans (1 μm per Z-step) are projected with 360-degree rotation for better visualization of spatial relation of the loaded viruses in MS particle (MP4 movie, Fig. S7). Virus loaded MS were stained with DAPI (excitation 405 nm; emission 425 nm), while a 561 nm laser excitation indicated polymer background autofluorescence (emission 590 nm). CLSM images showed the MS structure (red) with specks of viral particles (green) closer to the surface of the particles. This data reveals the inclusion of viral particles, possibly as aggregates, into the MS.

3.6. Functional immune responses to inactive SARS-CoV-2 antigen-loaded MS

3.6.1. Humoral immune response to MS delivered antigens

To evaluate the immunogenicity of the inactive SARS-CoV-2-loaded MS (MS-Ag), 10-week-old Sprague Dawley (SD) rats ($n = 6$, avg. weight = 270 g) were given single IM injection of 40 μg/g body weight MS-Ag, which was equivalent to 6 μg/g of inactive SARS-CoV-2 antigen. Blood samples were collected at 7- and 28-days post-injection (dpi), to quantify the serum IgG levels against SARS-CoV-2 spike (S) and nucleoprotein (N) (Fig. 6a). The blood collection timeline was chosen to reflect the immune responses that were demonstrated to arise post-COVID-19 vaccines in clinical trials [62,63] (NCT04852276). Presence of SARS-CoV-2 S-RBD or N-specific IgG antibodies were tested by ELISA (Fig. 6b). There was a significant increase in anti-SARS-CoV-2 S-RBD IgG responses in MS-Ag group (3369.9 ng/mL) compared to saline (58.8 ng/mL) and control MS (no antigen, 137.2 ng/mL) groups at day-28. An increasing trend of anti-SARS-CoV-2 S-RBD IgG responses was observed from day-7 (2061.23 ng/mL) today-28 within MS-Ag group was observed.

For SARS-CoV-2 N-IgG responses, significant SARS-CoV-2 N-IgG was seen at day-28 (38.85 ng/mL) compared to day 7 and without viral antigen controls (undetectable). This shows that the MS were able to deliver antigen *in vivo* to generate SARS-CoV-2 protein specific IgG as part of humoral responses.

3.6.2. Detection of T-lymphocytes following viral antigen immunization to SD rats

Besides humoral immune responses, the cellular arm of immunity confers an additional layer of protection against SARS-CoV-2 infection [64] and is a crucial determinant of vaccine efficacy. Also, the recognition of antigen by the spleen activates and induces the requisite T-cell activation signals in APCs, cytokine secretion, and pathogen clearance by phagocytes [65]. Therefore, the ability of the MS-Ag to elicit a cellular immune response to SARS-CoV-2 was assessed.

Specifically, the CD4+ and CD8+ cell responses in the splenocytes of the SD rats were analyzed by flow cytometry for both the treated ($n = 6$, for both empty MS and MS-Ag groups) and untreated ($n = 4$ for saline) groups. Fig. S8 showed the representative gating for flow cytometry analysis using the isotypes and fluorescence-minus-one (FMO) controls for each antibody.

Spleen-derived T-cells showed a significant increase in CD4+CD69+ activated T-cells (Fig. 7a), at 28 dpi for MS-Ag group, compared to the controls (Saline and MS only group). However, there was an increasing trend (not-significant) of CD8+CD69+ activated T-cells (Fig. 7b) in the treated group compared to the controls. The phenotype of the SARS-CoV-2-specific T-cell memory response during SARS-CoV-2 infection and post-vaccination has been characterized in human population [66,67]. CD62L/L-selectin is a marker found on naïve T-cells and further distinguishes central memory (T_{CM}, CD62L+) from effector memory (T_{EM}, CD62L−) T-cells [68]. In case of T_{CM} cell populations, there was a significant increase in both CD4+CD62L+CD44+ (Fig. 7c) and CD8+CD62L+CD44+ (Fig. 7d) T-cells populations compared to both the control groups, at 28 dpi. However, there were no changes in T_{EM} cell populations for the CD4+CD62L-CD44+ (Fig. S9a) and CD8+CD62L-CD44+ (Fig. S9b) T-cells at 28 dpi.

In addition to investigating the T-cell memory phenotypes in spleen, the nature of cytokine responses within splenocyte-derived CD4+ T-cell populations to the MS-based delivery of inactive SARS-CoV-2 antigen was investigated. The splenocytes were cultivated in presence of a specific S-peptide pool (to activate SARS-CoV-2 specific T-cells) and analyzed for the expression of the respective intracellular cytokines, IFNγ, IL4, and IL17 within CD4+ T-cell
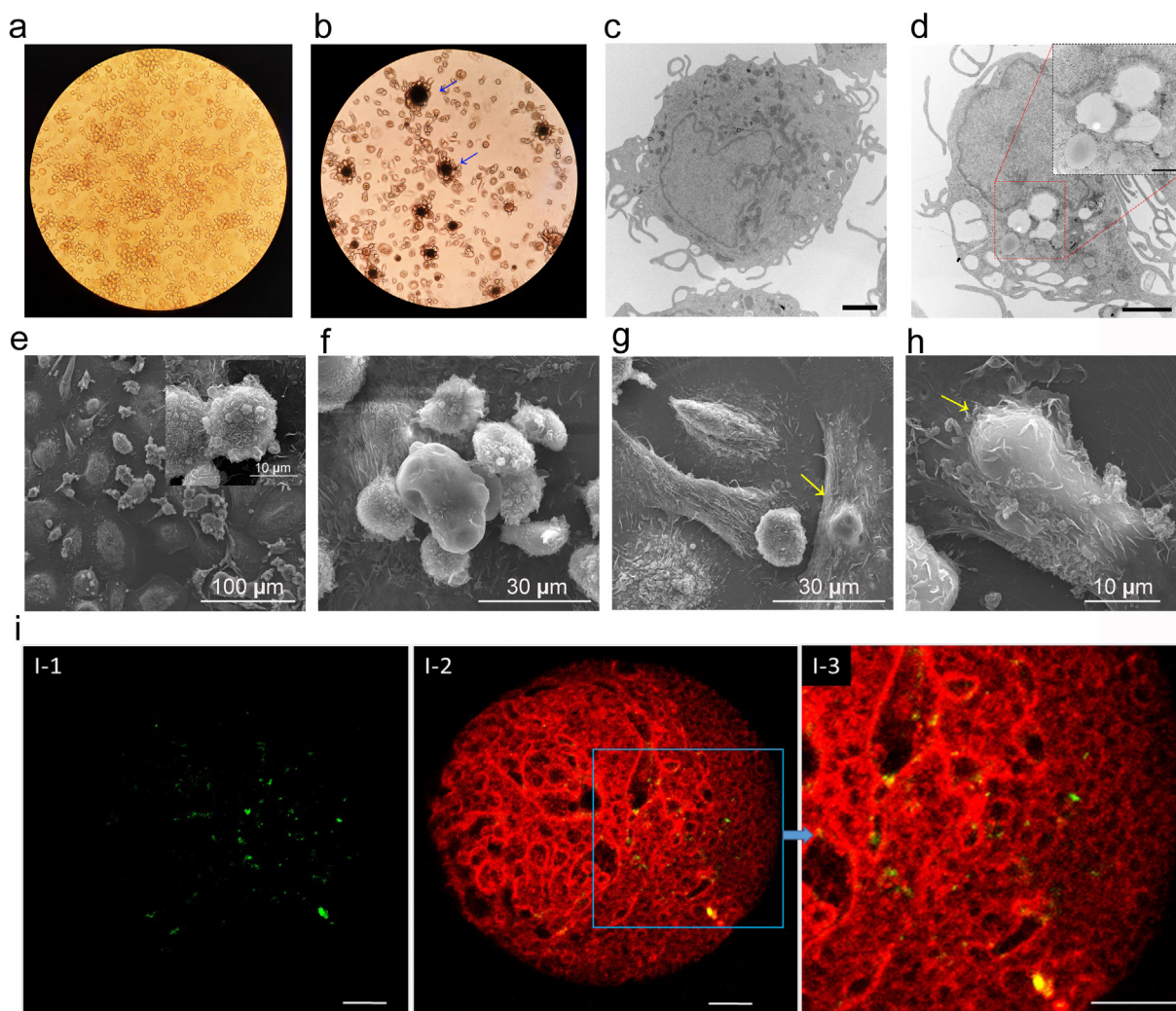
Fig. 5. Microscopic analysis of microsphere (MS)-macrophage interactions. Monocyte-derived macrophages (MDMs) (2×10^{-6}) were treated with 3 mg of multipolymer MS and incubated for 7 days. Light microscopy images, taken with 20x objective lenses, of (a) control MDMs, and (b) treated MDMs showed cells clustering around the multipolymer MS (blue arrows). Representative TEM images of (c) control and (d) MS SARS-CoV-2-treated macrophages showed vacant spherical compartments inside treated cells, indicating the regions where the MS resided upon intake. Scale bar: 2 μm. SEM images of (e) control MDMs, and (f-h) MS SARS-CoV-2-treated MDMs showed treated cell clusters around and the engulfed in MS (yellow arrows). (i) Confocal overlaid (MaxIP) image from 30 optical scan (Z step 1 μm) showing detected inactive SARS-CoV-2 viral particles stained with DAPI (excitation/emission: 405 nm/425 nm; panel i-1) and the merged images with MS autofluorescence (excitation/emission, 561 nm/590 nm, panel i-2). The panel i-3 is the portion of panel i-2 (the blue box) at higher magnification showing the viral particles (green/yellow) within the MS surface porous structures. Scale bar: 10 μm.

populations, reflective of the respective T_h1, T_h2, and T_h17 T-cell responses, respectively. Data revealed a substantial percentage of cells expressing each noted cytokine within CD4+ T-cells. For the MS-Ag group, there was a significant increase in the expression of CD4+IFNγ+ cells at 7 (Fig. 7e) and 28 dpi (Fig. 7f). Also, there was a significant increase in the CD4+IL-4+ cells expression at 28 dpi (Fig. 7g) but not earlier (Fig. S9c). There was an increasing trend in CD4+IL-17+ expressing T-cells at 7 dpi (Fig. S9d) and 28 dpi (Fig. 7h) for the MS-Ag group, while the control groups showed no significant differences. The data is congruent with the past literature of SARS-CoV-2 vaccination, demonstrating that the CD4+ responses exhibit a T_h1 profile [69,70] and are typically detectable by day-8 after a priming dose [67,71,72].

3.7. Toxicity profiles

Toxicity assessments were conducted for SD rats intramuscularly injected with saline, empty MS, or MS-Ag. The assessments consisted of collecting SD rat plasma and tissues for hematologic, serum chemistry and histopathological evaluations. Controls were age and sex-matched and evaluated in replicated untreated/saline treated rats. Erythema and edema were not observed at the site of injection in any of the microparticle injection groups. No significant hematological abnormalities were detected (Table 1), where total white cell, neutrophil, lymphocyte, and monocyte counts were all within the indicated ranges. There were no notable differences between MS and MS-Ag injected groups for comprehensive serum chemistry profile analysis except the level of ALP (214 ± 17.3 U/L for MS viral antigen group, 343.5 ± 55.8 U/L as compared to control group 261 ± 37.5 U/L) (Fig. S10), suggesting that the MS formulations did not adversely affect major organ functions. Hematoxylin and eosin-stained tissue sections were examined in a blinded fashion and revealed no abnormal pathology in the spleen, kidney, liver, and caudal thigh muscles of treated animals on 28 dpi (Fig. 8). There was no evidence of muscle degeneration or abscesses in any of the treatment groups. No significant injection site
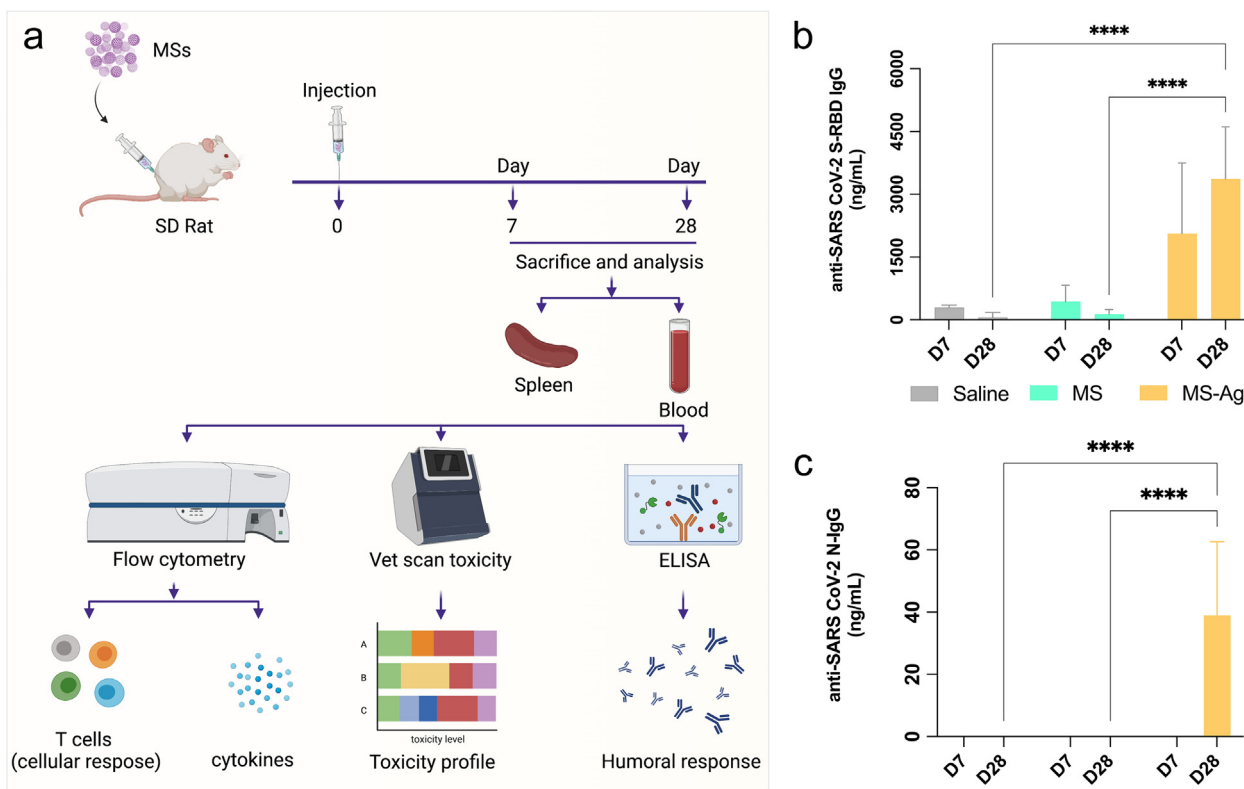
Fig. 6. Humoral immune response to MS-Ag administration in SD rats. (a) Experimental outline for the blood and organ collection, 7- and 28-days post-IM injection of SD rats with either saline, empty MS, or MS-Ag. Splenocytes were subjected to flow cytometry. Blood was analyzed for T-cell subsets and toxicity profiling, (b) Enzyme linked immunosorbent assay (ELISA) for (b) anti-SARS CoV2 S-RBD IgG and (c) Nucleoprotein (N) IgG response showed significant IgG production at day 28 for anti-SARS-CoV-2 S-RBD IgG and N-IgG. Statistical analysis was done by Two-way ANOVA and Tukey's post- hoc tests for multiple comparisons, (****$P < 0.0001$).

Table 1

Hematological toxicity assessments for complete blood cell counts. Plasma collected at 28 dpi, from SD rats given IM injections of either saline, MS, MS-Ag were evaluated for hematological toxicity using VetScan HM5 for complete blood count. Values reported are the mean ± SEM of 4 replicates for saline group and 6 replicates for MS formulation treated groups.

|	Saline	MS	MS-Ag	Range	
WBC	2.9 ± 0.7	4.8 ± 0.8	3.4 ± 0.8	2.1-19.5	10^9/L
LYM	1.8 ± 0.1	4.0 ± 0.6	2.7 ± 0.7	2-14.1	10^9/L
MON	0.1 ± 0.0	0.3 ± 0.1	0.1 ± 0.1	0-0.98	10^9/L
NEU	0.3 ± 0.1	0.6 ± 0.2	0.5 ± 0.2	0.1-5.4	10^9/L
LYM%	86.1 ± 2.4	85.1 ± 2.6	76.1 ± 5.5	55-97	%
MON%	3.1 ± 1.2	5.4 ± 1.3	6.7 ± 1.5	0-5	%
NEU%	10.9 ± 3.0	9.6 ± 1.6	17.1 ± 5.0	2-31.0	%
RBC	1.2 ± 0.1	0.9 ± 0.1	0.9 ± 0.0	5.3-10	10^{12}/L
HGB	20.7 ± 1.4	17.6 ± 0.7	16.1 ± 0.2	14-18	g/dL
HCT	68.7 ± 4.3	51.8 ± 0.6	50.3 ± 1.0	35-52	%
MCV	59.5 ± 2.5	56.5 ± 3.5	58 ± 0.0	50-62	fl
MCH	19.4 ± 0.1	17.7 ± 0.8	18.1 ± 0.2	16-23	pg
MCHC	32.7 ± 1.3	31.2 ± 0.6	31 ± 0.3	31-40	g/dL
RDWc	16.7 ± 1	16.4 ± 0.3	15.6 ± 0.2		%
RDWs	37.9 ± 0.4	36.0 ± 1.6	34.8 ± 0.4		10^9/L

reactions were observed at the site of MS injection with or without viral antigens.

4. Discussion

Biodegradable polymer-based sustained release cargo delivery systems are an attractive alternative to therapeutic protein delivery. For vaccination regimes, this approach can reduce the administration frequency by combining the priming and booster doses into a single formulation. This method allows for a sus-

tained antigen release for continued protective immunity, as the injected polymer-cargo undergo phagocytosis by the APCs to induce an effective immune responses [73]. The beneficial prospects of polymer-based delivery systems lie in its recognition for affecting immune cell interactions. From that base, an injectable, porous MS of a multipolymer blend carrying antigen was developed and injected for a "proof-of-concept" evaluation of antigen delivery for generating effective antiviral immunity. The multipolymer blend is intended to confer the advantage of early and late release of its payload by being composed of fast and slow degrading components. Specifically, the MS were composed of FDA-approved biodegradable PLLA, PLGA, and PCL polymers. Formulations with the single polymer MS were investigated in the past for the preparation of peptides, drug, and gene therapy delivery systems [74–77]. These polymers can be fabricated into various morphologies and sizes to generate nano- and microspheres. This offers the potential for tailoring a versatile controlled long-acting release of therapeutic cargo with optimal therapeutic outcomes.

The porous multipolymer MS was produced reproducibly. It showed a 'patchy' polymer distribution with a thin layer of PLGA on the surface and an internal matrix of PCL. This polymer distribution would allow for the PLGA to degrade first and followed by PCL, providing a two-phase release profile. The multipolymer MS provides an alternative delivery method of microencapsulated peptide and protein antigens. Previous studies have explored antigen delivery to APCs for sustained immunity [1,73,78]. Therefore, it is important to test whether this platform can include and then deliver such cargo at a modulatory rate for improving time-dependent immunogenicity. We have thoroughly characterized the morphological and thermal stability of the MS, and its ability to carry antigen. The CLSM data showed the presence of vi-
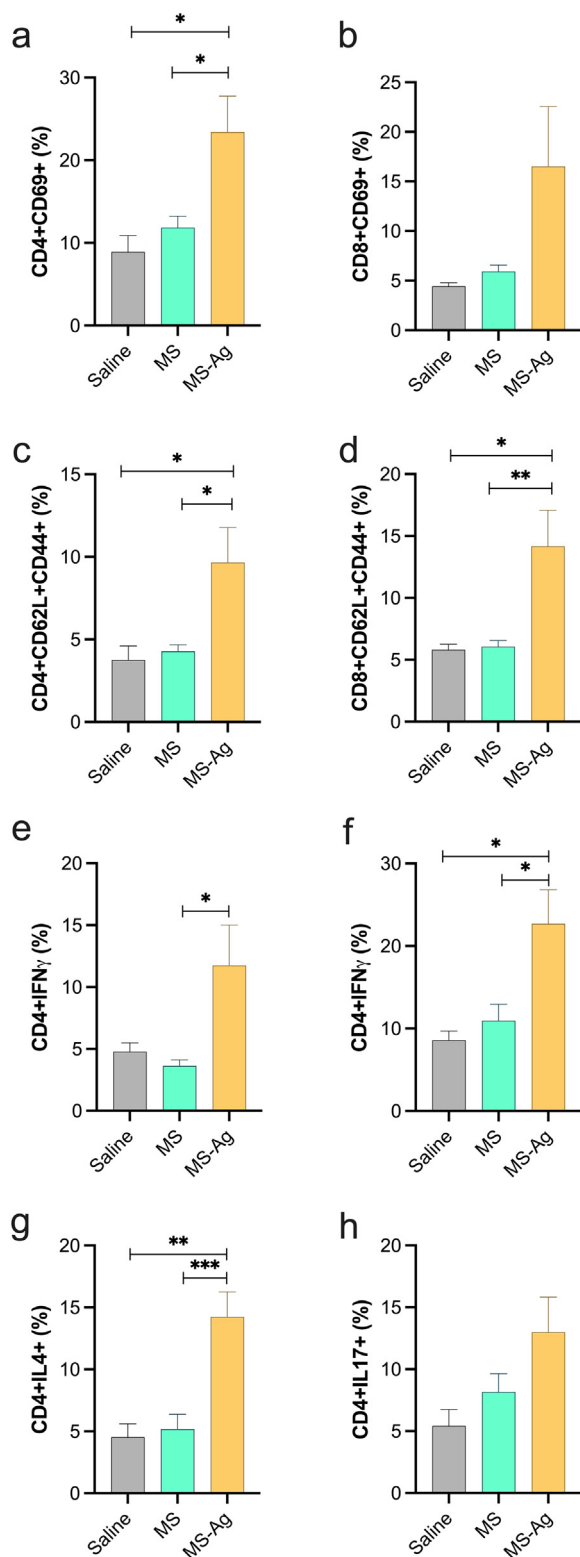
Fig. 7. Cellular immune response to MS-Ag administration in SD rats. SD rats (average body weight = 270 g) were each injected with a single intramuscular dose of 6 µg/g of body weight of chemically inactivated SARS-CoV-2 loaded MS (MS-Ag). From SD rats injected with MS-Ag, empty MS or saline, T-cell subsets of splenocytes were analyzed at 7 and 28 dpi by flow cytometry. (a-b) Percentage population of activated T-cells (CD4+CD69+ and CD8+CD69+), 28 dpi. (c-d) Percentage population of TCM - cells (CD4+CD62L+CD44+ and CD8+CD62L+CD44+), 28 dpi. Intracellular cytokine staining and flow cytometric analysis of CD4+ T-cell subset expressing (e) IFNγ at 7 dpi, (f) IFNγ at 28 dpi, (g) IL4 at 28 dpi, and (h) IL17 at 28 dpi. Statistical analysis was done by One-way ANOVA followed by Newman/Keul's post-hoc analysis for multiple comparisons, (*$P < 0.05$; **$P < 0.01$; ***$P < 0.001$). Abbreviations: MS, multipolymer microsphere; Ag, antigen; IFNγ, Interferon-gamma; IL, Interleukin; %, percentage of the parent population.

ral particles, possibly as aggregates, close to the MS surface, proving successful loading. Due to limitations of staining penetrability within the MS, visualization of bulk viral loading was not possible. Limitations exist for viral aggregation highlighting the needs to improve the physical and chemical antigen stability. Such stability is critical to the immunogenicity of the embedded and released antigen [79]. *First*, researchers are still exploring the most effective β-propiolactone concentration or alternative inactivators for viral inactivation that may reduce the occurrence of viral aggregation [80,81]. *Second*, the length of peptide/protein exposure to the organic solvent interface may affect its surface properties that drive the aggregation [73,82] during preparation. To overcome the aggregation related issues and improve the potential antigen stability during production, recommended strategies included co-encapsulation of stabilizing additives, physicochemical stabilization of the antigen itself, or solid-state microencapsulation [73,83–87]. In hopes of reducing the abrasive effects on the antigen, this process limited the use of organic solvents during the emulsion formation of the solvent evaporation process. This adjustment involved co-mixing higher boiling point solvents to reduce the quantity of the organic phase, which delayed the phase-inversion which rendered smaller MS that still encapsulated the antigen.

Considering the previously stated issues with antigen stability, the most important criteria is to develop a delivery system capable of delivering the entrapped material in a bioactive form. Meaning the cargo within the MS must be in a fully immunogenic form of the antigen if the system needs to be used as an effective vaccine platform. It is widely known that a vaccination leverages the biology of antigenic imprinting by the B- and T-cells upon initial pathogen exposure and aids in shaping the immune response to subsequent re-infections. For SARS-CoV-2, both humoral and adaptive immune responses are determinants of the clinical outcome of viral infection [88]. Therefore, SARS-CoV-2 IgG and adaptive immune activities that are known to be generated in response to vaccination were evaluated to determine the functionality of antigen (SARS-CoV-2) loaded multipolymer MS as a 'proof-of-concept' of bioactivity.

Previous observational studies for humoral immune responses demonstrated that IgG antibodies, specific for SARS-CoV-2 S and N proteins typically became detectable in infected human patients' blood at median times of about 2 weeks after onset of COVID-19 symptoms [89–91]. Also, outpatients and non-ICU inpatients show preferential IgG antibody targeting of a spike (RBD and S1 subunit) compared to the N protein [89]. Also, irrespective of the chosen immunization regime, vaccinated individuals showed detectable IgG antibodies 2 weeks after the second vaccine dose indicating the development of a robust humoral immunity [92]. Our preliminary study also demonstrates the successful IgG responses against the anti-SARS-CoV-2 spike-RBD protein in greater magnitude than against N protein. Future viral neutralization assays will be able to determine the extent of antigen neutralization capacity by the plasma IgG produced in response to the SARS-CoV-2 encapsulated MS.

Moreover, a literature review of phenotypic characterization of T lymphocytes (for cellular immune responses) indicates that in the case of SARS-CoV-2 infection, CD4+ T cell responses were greater than the CD8+ T cells, which may further increase over time [66]. Mostly CD4+ Th1, with characteristics of effector (T$_{EM}$) or central (T$_{CM}$) memory cells [66,93,94] are observed, which were primarily CD4+ T$_{CM}$ profiles, all of which augur well for longevity of responses [66]. All of the abovementioned reports were aligned with our observations in this study, where the T-cell profiles post-MS-Ag administration reflect that of the natural infection [88]. However, the magnitude of anti-SARS-CoV-2 epitope-specific T cell induction that can be achieved by the MS-Ag has yet to be fully determined. Past reports suggest that SARS-CoV-2 IgG, and epitope-
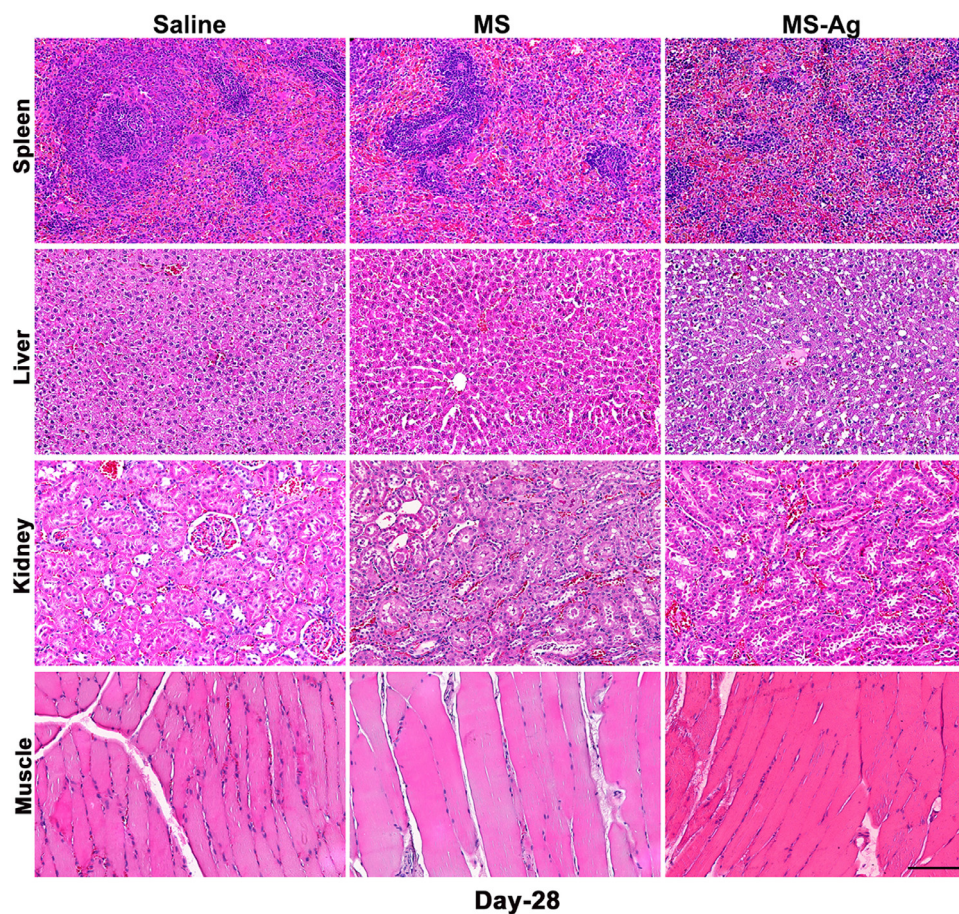
Fig. 8. Tissue histology of SD rats upon MS-Ag treatment. Hematoxylin and eosin staining of representative sections from liver, kidney, muscle (injection site) and spleen tissues in untreated (saline injection), empty MS and MS-Ag injected SD rats at the endpoint (28 days post-injection) of the study. No tissue pathology was observed in MS and MS-Ag groups as compared to untreated/saline injected controls. The images were captured at 20x magnification. Scale bar is 100μm.

specific T cell induction varies by the vaccine platform [95,96]. Heterologous vaccine platforms [97] were also explored to combine the benefits of the different vaccine types, although short-term vaccine side effects were somewhat higher with this approach [98] New formulations, including peptide formulations, are also being assessed [99] Regardless of the approaches currently available, the injectable biodegradable polymer MS represents an important approach to obtaining a controlled release of vaccine antigens, which in turn has shown to reduce doses needed for immunization [100].

Polymer-based MS as a drug delivery system have an impressive safety record in humans. It is anticipated that multipolymer MS will be an excellent platform to provide sustained release of vaccine antigens for improved immunogenic responses. Key clinical question in the ongoing COVID-19 pandemic is the extent of patient's humoral (B-cell and antibody-based) [92] and cellular (T-cell and cytokine based) responses. This notion drives the search for effective vaccine candidates, comparing the vaccine-induced immune responses to those stimulated by viral infection. Many different vaccine categories have been studied with some acquiring US Food and Drug Administration (FDA)-approval in 2021 [101]. However, the protective efficacy of current vaccines against infection and re-infection and the duration of protection in real life, are still unclear. Therefore, the MS-Ag demonstrated a proof-of-concept for the successful loading and potential immunogenic responses to the whole, inactive virus. Future studies to optimize the process parameters to generate MS viral antigens, as well as a long-term study of the im-

mune responses against the antigen of interest, will provide the opportunity for developing a long-acting vaccine.

5. Conclusion

A potential sustained release MS platform can be influenced by factors such as polymer types and blends, porosity, and route of in vivo administration. The blending of hydrophilic, amorphous polymers to hydrophobic, crystalline polymers may improve the peptide-protein microencapsulation [102,103], or adjust the antigen release [104]. Miscible polymers were combined to rely on its complementing properties – degradation and release rates, hydrophilicity-hydrophobicity, and reported compatibility with antigen – to generate a MS that undergoes sustained degradation and antigen (whole, inactive SARS-CoV-2) release to elicit humoral (B-cell and antibody production) and cellular (memory cell generation) responses for protective immunity. Future studies, accounting for improved antigen inactivation, optimized antigen stability and release with the best manufacturing and storage conditions [105] must be performed. All can exploit the multipolymer blend designs for effective single-dose vaccines.

Contributors

F.S. and M.P. devised and planned the experimental approaches; F.S., M.P., B.D.K., J.M., I.A., Y.Z., J.D.C., M.U.N., P.D., C.Z., E.W., P.Y., and M.M. performed the experiments; F.S., M.P., B.D.K, J.M. and

Declaration of Competing Interest

F.S., M.P., B.D.K and H.E.G. are named inventors on provisional patents for the porogen used, MS composition and antigen loading, and delivery as described in this report (63/286,304, 63/158,484). F.S., M.P., B.D.K and H.E.G. hold a patent on 'Microparticle compositions and methods use thereof' (Docket No. 21069PCT, Serial No. PCT/US2022/01950, International Publication No. WO2022192361A2). H.E.G is a member of the scientific advisory board at Longevity Biotech and a co-founder of Exavir Therapeutics, Inc.

Acknowledgments

Supplementary materials

Supplementary material associated with this article can be found, in the online version, at doi:10.1016/j.actbio.2022.12.043.

References

[1] C.Y. Lin, S.J. Lin, Y.C. Yang, D.Y. Wang, H.F. Cheng, M.K. Yeh, Biodegradable polymeric microsphere-based vaccines and their applications in infectious diseases, Hum. Vaccin. Immunother. 11 (3) (2015) 650–656.

[2] H. Tamber, P. Johansen, H.P. Merkle, B. Gander, Formulation aspects of biodegradable polymeric microspheres for antigen delivery, Adv. Drug. Deliv. Rev. 57 (3) (2005) 357–376.

[3] M.T. Aguado, P.H. Lambert, Controlled-release vaccines-biodegradable polylactide/polyglycolide (PL/PG) microspheres as antigen vehicles, Immunobiology 184 (2) (1992) 113–125.

[4] J.L. Cleland, L. Barrón, P.W. Berman, A. Daugherty, T. Gregory, A. Lim, J. Vennari, T. Wrin, M.F. Powell, Development of a single-shot subunit vaccine for HIV-1. 2. defining optimal autoboost characteristics to maximize the humoral immune response, J. Pharm. Sci. 85 (12) (1996) 1346–1349.

[5] M. Ying, B. Gander, H.P. Merkle, G. Corradin, Induction of sustained and elevated immune responses to weakly immunogenic synthetic malarial peptides by encapsulation in biodegradable polymer microspheres, Vaccine 14 (15) (1996) 1442–1450.

[6] C. Thomasin, G. Corradin, Y. Men, H.P. Merkle, B. Gander, Tetanus toxoid and synthetic malaria antigen containing poly(lactide)/poly(lactide-co-glycolide) microspheres: importance of polymer degradation and antigen release for immune response, J. Control. Release 41 (1) (1996) 131–145.

[7] R. Guarecuco, J. Lu, K.J. McHugh, J.J. Norman, L.S. Thapa, E. Lydon, R. Langer, A. Jaklenec, Immunogenicity of pulsatile-release PLGA microspheres for single-injection vaccination, Vaccine 36 (22) (2018) 3161–3168.

[8] J.L. Cleland, A. Lim, L. Barrón, E.T. Duenas, M.F. Powell, Development of a single-shot subunit vaccine for HIV-1: Part 4. Optimizing microencapsulation and pulsatile release of MN rgp120 from biodegradable microspheres, J. Control. Release 47 (2) (1997) 135–150.

[9] A.K. Hilbert, U. Fritzsche, T. Kissel, Biodegradable microspheres containing influenza a vaccine: immune response in mice, Vaccine 17 (9-10) (1999) 1065–1073.

[10] L.J. Cruz, P.J. Tacken, F. Rueda, J.C. Domingo, F. Albericio, C.G. Figdor, Chapter eight - targeting nanoparticles to dendritic cells for immunotherapy, in: Methods in Enzymology, Academic Press, 2012, pp. 143–163.

[11] R. Han, J. Zhu, X. Yang, H. Xu, Surface modification of poly(D,L-lactic-co-glycolic acid) nanoparticles with protamine enhanced cross-presentation of encapsulated ovalbumin by bone marrow-derived dendritic cells, J. Biomed. Mater. Res. Part A 96 1 (2011) 142–149.

[12] F. Khademi, M. Derakhshan, A. Yousefi-Avarvand, M. Tafaghodi, Potential of polymeric particles as future vaccine delivery systems/adjuvants for parenteral and non-parenteral immunization against tuberculosis: a systematic review, Iran. J. Basic. Med. Sci. 21 (2) (2018) 116–123.

[13] J. Han, D. Zhao, D. Li, X. Wang, Z. Jin, K. Zhao, Polymer-based nanomaterials and applications for vaccines and drugs, Polymers 10 (1) (2018) 31.

[14] Y. Waeckerle-Men, E.U.V. Allmen, B. Gander, E. Scandella, E. Schlosser, G. Schmidtke, H.P. Merkle, M. Groettrup, Encapsulation of proteins and peptides into biodegradable poly(D,L-lactide-co-glycolide) microspheres prolongs and enhances antigen presentation by human dendritic cells, Vaccine 24 11 (2006) 1847–1857.

[15] S. Prior, B. Gander, N. Blarer, H.P. Merkle, M.A.L. Subirá, J.M. Irache, C. Gamazo, *In vitro* phagocytosis and monocyte-macrophage activation with poly(lactide) and poly(lactide-co-glycolide) microspheres, Eur. J. Pharm. Sci. 15 (2) (2002) 197–207.

[16] B. Sanders, M. Koldijk, H. Schuitemaker, Inactivated Viral Vaccines, Vaccine Anal. Strategies Princ. Control (2014) 45–80.

[17] L. Zhang, W. Yang, C. Hu, Q. Wang, Y. Wu, Properties and applications of nanoparticle/microparticle conveyors with adjuvant characteristics suitable for oral vaccination, Int. J. Nanomed. 13 (2018) 2973–2987.

[18] X. Hong, X. Zhong, G. Du, Y. Hou, Y. Zhang, Z. Zhang, T. Gong, L. Zhang, X. Sun, The pore size of mesoporous silica nanoparticles regulates their antigen delivery efficiency, Sci. Adv. 6 (25) (2020) eaaz4462.

[19] E.J. Mendoza, K. Manguiat, H. Wood, M. Drebot, Two detailed plaque assay protocols for the quantification of infectious SARS-CoV-2, Curr. Protoc. Microbiol. 57 (1) (2020) cpmc105.

[20] M.M. Abdelmoaty, P. Yeapuri, J. Machhi, K.E. Olson, F. Shahjin, V. Kumar, Y. Zhou, J. Liang, K. Pandey, A. Acharya, S.N. Byrareddy, R.L. Mosley, H.E. Gendelman, Defining the innate immune responses for SARS-CoV-2-human macrophage interactions, Front. Immunol. 12 (2021).

[21] F. Shahjin, R.S. Guda, V.L. Schaal, K. Odegaard, A. Clark, A. Gowen, P. Xiao, S.J. Lisco, G. Pendyala, S.V. Yelamanchili, Brain-derived extracellular vesicle microRNA signatures associated with in utero and postnatal oxycodone exposure, Cells 9 (1) (2019).

[22] Y.L. Lyubchenko, A.A. Gall, L.S. Shlyakhtenko, Visualization of DNA and protein-DNA complexes with atomic force microscopy, Methods Mol. Biol. 1117 (2014) 367–384.

[23] L.S. Shlyakhtenko, A.A. Gall, A. Filonov, Z. Cerovac, A. Lushnikov, Y.L. Lyubchenko, Silatrane-based surface chemistry for immobilization of DNA, protein-DNA complexes and other biological materials, Ultramicroscopy 97 (1) (2003) 279–287.

[24] J. Schindelin, I. Arganda-Carreras, E. Frise, V. Kaynig, M. Longair, T. Pietzsch, S. Preibisch, C. Rueden, S. Saalfeld, B. Schmid, J.Y. Tinevez, D.J. White, V. Hartenstein, K. Eliceiri, P. Tomancak, A. Cardona, Fiji: an open-source platform for biological-image analysis, Nat. Methods 9 (7) (2012) 676–682.

[25] N. Otsu, A threshold selection method from gray-level histograms, IEEE Trans. Syst. Man Cybern. 9 (1) (1979) 62–66.

[26] D.A. Cobb, N. Smith, S. Deodhar, A.N. Bade, N. Gautam, B.L.D. Shetty, J. McMillan, Y. Alnouti, S.M. Cohen, H.E. Gendelman, B. Edagwa, Transformation of tenofovir into stable ProTide nanocrystals with long-acting pharmacokinetic profiles, Nat. Commun. 12 (1) (2021) 5458 -5458.

[27] B.D. Kevadiya, B. Ottemann, I.Z. Mukadam, L. Castellanos, K. Sikora, J.R. Hilaire, J. Machhi, J. Herskovitz, D. Soni, M. Hasan, W. Zhang, S. Anandakumar, J. Garrison, J. McMillan, B. Edagwa, R.L. Mosley, R.W. Vachet, H.E. Gendelman, Rod-shape theranostic nanoparticles facilitate antiretroviral drug biodistribution and activity in human immunodeficiency virus susceptible cells and tissues, Theranostics 10 (2) (2020) 630–656.

[28] I.Z. Mukadam, J. Machhi, J. Herskovitz, M. Hasan, M.D. Oleynikov, W.R. Blomberg, D. Svechkarev, A.M. Mohs, Y. Zhou, P. Dash, J. McMillan, S. Gorantla, J. Garrison, H.E. Gendelman, B.D. Kevadiya, Rilpivirine-associated aggregation-induced emission enables cell-based nanoparticle tracking, Biomaterials 231 (2020) 119669 -119669.

[29] A.D. Murdin, L. Barreto, S. Plotkin, Inactivated poliovirus vaccine: past and present experience, Vaccine 14 (8) (1996) 735–746.

[30] C. Vellozzi, D.R. Burwen, A. Dobardzic, R. Ball, K. Walton, P. Haber, Safety of trivalent inactivated influenza vaccines in adults: background for pandemic influenza vaccine safety monitoring, Vaccine 27 (15) (2009) 2114–2120.

[31] A.S. Jureka, J.A. Silvas, C.F. Basler, Propagation, Inactivation, and safety testing of SARS-CoV-2, Viruses 12 (6) (2020) 622.

[32] S. Lyonnais, M. Hénaut, A. Neyret, P. Merida, C. Cazevieille, N. Gros, C. Chable-Bessia, D. Muriaux, Atomic force microscopy analysis of native infectious and inactivated SARS-CoV-2 virions, Sci. Rep. 11 (1) (2021) 11885.

[33] D.V. Bagrov, G.S. Glukhov, A.V. Moiseenko, M.G. Karlova, D.S. Litvinov, P. Zaitsev, L.I. Kozlovskaya, A.A. Shishova, A.A. Kovpak, Y.Y. Ivin, A.N. Piniaeva, A.S. Oksanich, V.P. Volok, D.I. Osolodkin, A.A. Ishmukhametov, A.M. Egorov, K.V. Shaitan, M.P. Kirpichnikov, O.S. Sokolova, Structural characterization of β-propiolactone inactivated severe acute respiratory syndrome coronavirus 2 (SARS-CoV-2) particles, Microsc. Res. Tech. 85 (2) (2022) 562–569.

[34] N.K. Dutta, K. Mazumdar, J.T. Gordy, The nucleocapsid protein of SARS-CoV-2: a target for vaccine development, J. Virol. 94 (13) (2020) e00647 -20.

[35] L. Dai, G.F. Gao, Viral targets for vaccines against COVID-19, Nat. Rev. Immunol. 21 (2) (2021) 73–82.

[36] E.K. Loveday, K.S. Hain, I. Kochetkova, J.F. Hedges, A. Robison, D.T. Snyder, S.K. Brumfield, M.J. Young, M.A. Jutila, C.B. Chang, M.P. Taylor, Effect of inactivation methods on SARS-CoV-2 virion protein and structure, Viruses 13 (4) (2021) 562.

[37] B. Amoyav, O. Benny, Microfluidic based fabrication and characterization of highly porous polymeric microspheres, Polymers 11 (3) (2019) 419 (Basel).

[38] D. Klose, F. Siepmann, K. Elkharraz, S. Krenzlin, J. Siepmann, How porosity and size affect the drug release mechanisms from PLGA-based microparticles, Int. J. Pharm. 314 (2) (2006) 198–206.

[39] S.A. Chew, M.A. Arriaga, V.A. Hinojosa, Effects of surface area to volume ratio of PLGA scaffolds with different architectures on scaffold degradation characteristics and drug release kinetics, J. Biomed. Mater. Res. A 104 (5) (2016) 1202–1211.

[40] C.D.A.C. Erbetta, R.J. Alves, J. Magalh, R.F. de Souza Freitas, R.G. de Sousa, Synthesis and Characterization of Poly (D, L-Lactide-Co-Glycolide) Copolymer, (2012).

[41] T. Kaur, R. Kaur, A. Kaur, Recent biomedical applications and patents on biodegradable polymer, 2014.

[42] T.C. Taucher, I. Hehn, O.T. Hofmann, M. Zharnikov, E. Zojer, Understanding chemical versus electrostatic shifts in X-ray photoelectron spectra of organic self-assembled monolayers, J. Phys. Chem. C 120 (6) (2016) 3428–3437.

[43] E. Korin, N. Froumin, S. Cohen, Surface analysis of nanocomplexes by X-ray photoelectron spectroscopy (XPS), ACS Biomater. Sci. Eng. 3 (6) (2017) 882–889.

[44] Z. Esmaili, S. Bayrami, F.A. Dorkoosh, H. Akbari Javar, E. Seyedjafari, S.S. Zargarian, V. Haddadi-Asl, Development and characterization of electrosprayed nanoparticles for encapsulation of Curcumin, J. Biomed. Mater. Res. Part A 106 (1) (2018) 285–292.

[45] Z.A. Abdul Hamid, C.Y. Tham, Z. Ahmad, Preparation and optimization of surface-engineered poly(lactic acid) microspheres as a drug delivery device, J. Mater. Sci. 53 (7) (2018) 4745–4758.

[46] S. Bhatt, J. Pulpytel, M. Mirshahi, F. Arefi-Khonsari, Catalyst-free plasma-assisted copolymerization of Poly(ε-caprolactone)-poly(ethylene glycol) for biomedical applications, ACS Macro Lett. 1 (6) (2012) 764–767.

[47] P.L.J. Gunter, O.L.J. Gijzeman, J.W. Niemantsverdriet, Surface roughness effects in quantitative XPS: magic angle for determining overlayer thickness, Appl. Surf. Sci. 115 (4) (1997) 342–346.

[48] K. Vutova, G. Mladenov, T. Tanaka, K. Kawabata, Photoelectron signal simulation from textured samples covered by a thin film, Vacuum 62 (2) (2001) 297–302.

[49] P. Kappen, K. Reihs, C. Seidel, M. Voetz, H. Fuchs, Overlayer thickness determination by angular dependent X-ray photoelectron spectroscopy (ADXPS) of rough surfaces with a spherical topography, Surf. Sci. 465 (1) (2000) 40–50.

[50] S. Nojima, T. Shinohara, Y. Higaki, R. Ishige, T. Ohishi, D. Kobayashi, H. Setoyama, A. Takahara, Precise characterization of outermost surface of crystalline–crystalline diblock copolymer thin films using synchrotron radiation soft X-ray photoelectron spectroscopy, Polym. J. 46 (10) (2014) 637–640.

[51] G.P. López, D.G. Castner, B.D. Ratner, XPS O 1s binding energies for polymers containing hydroxyl, ether, ketone and ester groups, Surf. Interface Anal. 17 (1991) 267–272.

[52] M. Ayyoob, Y.J. Kim, Effect of chemical composition variant and oxygen plasma treatments on the wettability of PLGA thin films, synthesized by direct copolycondensation, Polymers 10 (10) (2018) 1132.

[53] J. Palacios, C. Albano, G. González, R.V. Castillo, A. Karam, M. Covis, Characterization and thermal degradation of poly(d,l-lactide-co-glycolide) composites with nanofillers, Polym. Eng. Sci. 53 (7) (2013) 1414–1429.

[54] O. Persenaire, M. Alexandre, P. Degée, P. Dubois, Mechanisms and kinetics of thermal degradation of poly(ε-caprolactone), Biomacromolecules 2 (1) (2001) 288–294.

[55] L.Y. Chu, L. Ye, K. Dong, R.W. Compans, C. Yang, M.R. Prausnitz, Enhanced stability of inactivated influenza vaccine encapsulated in dissolving microneedle patches, Pharm. Res. 33 (4) (2016) 868–878.

[56] Lyophilization and the thermostability of vaccines, Cell Preserv. Technol. 1 (2) (2002) 91–104.

[57] J.A. Champion, A. Walker, S. Mitragotri, Role of particle size in phagocytosis of polymeric microspheres, Pharm. Res. 25 (8) (2008) 1815–1821.

[58] C. Jiang, L. Kuang, M. Merkel, F. Yue, M. Cano-Vega, N. Narayanan, S. Kuang, M. Deng, Biodegradable polymeric microsphere-based drug delivery for inductive browning of fat, Front. Endocrinol. 6 (2015).

[59] Y. Kim, E.J. Park, T.W. Kim, D.H. Na, Recent progress in drug release testing methods of biopolymeric particulate system, Pharmaceutics 13 (8) (2021).

[60] Z. Liu, W. Ye, J. Zheng, Q. Wang, G. Ma, H. Liu, X. Wang, Hierarchically electrospraying a PLGA@chitosan sphere-in-sphere composite microsphere for multi-drug-controlled release, Regen. Biomater. 7 (4) (2020) 381–390.

[61] J. Li, L. Yang, C. Zhu, T. Peng, D. Huang, X. Ma, X. Pan, C. Wu, Release mechanisms of bovine serum albumin loaded-PLGA microspheres prepared by ultra-fine particle processing system, Drug Deliv. Transl. Res. 10 (5) (2020) 1267–1277.

[62] K.J. Ewer, J.R. Barrett, S. Belij-Rammerstorfer, H. Sharpe, R. Makinson, R. Morter, A. Flaxman, D. Wright, D. Bellamy, M. Bittaye, C. Dold, N.M. Provine, J. Aboagye, J. Fowler, S.E. Silk, J. Alderson, P.K. Aley, B. Angus, E. Berrie, S. Bibi, P. Cicconi, E.A. Clutterbuck, I. Chelysheva, P.M. Folegatti, M. Fuskova, C.M. Green, D. Jenkin, S. Kerridge, A. Lawrie, A.M. Minassian, M. Moore, Y. Mujadidi, E. Plested, I. Poulton, M.N. Ramasamy, H. Robinson, R. Song, M.D. Snape, R. Tarrant, M. Voysey, M.E.E. Watson, A.D. Douglas, A.V.S. Hill, S.C. Gilbert, A.J. Pollard, T. Lambe, A. Ali, E. Allen, M. Baker, E. Barnes, N. Borthwick, A. Boyd, C. Brown-O'Sullivan, J. Burgoyne, N. Byard, I.C. Puig, F. Cappuccini, J.S. Cho, P. Cicconi, E. Clark, W.E.M. Crocker, M.S. Datoo, H. Davies, F.R. Donnellan, S.J. Dunachie, N.J. Edwards, S.C. Elias, J. Furze, C. Gilbride, G. Gorini, G. Gupta, S.A. Harris, S.H.C. Hodgson, M.M. Hou, S. Jackson, K. Jones, R. Kailath, L. King, C.W. Larkworthy, Y. Li, A.M. Lias, A. Linder, S. Lipworth, R.L. Ramon, M. Madhavan, E. Marlow, J.L. Marshall, A.J. Mentzer, H. Morrison, N. Moya, E. Mukhopadhyay, A. Noé, F.L. Nugent, D. Pipini, D. Pulido-Gomez, F.R. Lopez, A.J. Ritchie, I. Rudiansyah, S. Salvador, H. Sanders, I. Satti, A. Shea, S. Silk, A.J. Spencer, R. Tanner, I.J. Taylor, Y. Themistocleous, M. Thomas, N. Tran, A. Truby, C. Turner, N. Turner, M. Ulaszewska, A.T. Worth, L. Kingham-Page, M.P.P. Alvarez, R. Anslow, L. Bates, K. Beadon, R. Beckley, A. Beveridge, E.M. Bijker, L. Blackwell, J. Burbage, S. Camara, M. Carr, R. Colin-Jones, R. Cooper, C.J. Cunningham, T. Demissie, C.D. Maso, N. Douglas, R. Drake-Brockman, R.E. Drury, K.R.W. Emary, S. Felle, S. Feng, C.F.D. Silva, K.J. Ford, E. Francis, L. Gracie, J. Hamlyn, B. Hanumunthadu, D. Harrison, T.C. Hart, S. Hawkins, J. Hill, E. Howe, N. Howell, E. Jones, J. Keen, S. Kelly, D. Kerr, L. Khan, J. Kinch, S. Koleva, E.A. Lees, A. Lelliott, X. Liu, N.G. Marchevsky, S. Marinou, J. McEwan, E. Morey, G. Morshead, J. Muller, C. Munro, S. Murphy, P. Mweu, E. Nuthall, K. O'Brien, D. O'Connor, P.J. O'Reilly, B. Oguti, P. Osborne, N. Owino, K. Parker, K. Pfafferott, D. Phillips, S. Provstgaard-Morys, H. Ratcliffe, T. Rawlinson, S. Rhead, H. Roberts, K. Sanders, L. Silva-Reyes, C.S. Rollier, C.C. Smith, D.J. Smith, L. Stockdale, A. Szigeti, T.M. Thomas, A. Thompson, A. Tomic, S. Tonks, R. Varughese, M.K. Verheul, I. Vichos, L. Walker, C. White, R. White, X.L. Yao, C.P. Conlon, J. Frater, L. Cifuentes, I. Baleanu, E. Bolam, E. Boland, T. Brenner, B.E. Damratoski, C. Datta, O.E. Muhanna, R. Fisher, P. Galian-Rubio, G. Hodges, F. Jackson, S. Liu, L. Loew, R. Morgans, S.J. Morris, V. Olchawski, C. Oliveria, H. Parracho, E.R. Pabon, A. Tahiri-Alaoui, K. Taylor, P. Williams, D. Zizi, E.H. Arbe-Barnes, P. Baker, A. Batten, C. Downing, J. Drake, M.R. English, J.A. Henry, P. Iveson, A. Killen, T.B. King, J.P.J. Larwood, G. Mallett, K. Mansatta, N. Mirtorabi, M. Patrick–Smith, J. Perring, K. Radia, S. Roche, E. Schofield, R.T.W. Naude, E. Towner, N. Baker, K.R. Bewley, E. Brunt, K.R. Buttigieg, M.W. Carroll, S. Charlton, N.S. Coombes, M.J. Elmore, K. Godwin, B. Hallis, D. Knott, L. McInroy, I. Shaik, K. Thomas, J.A. Tree, C.L. Blundell, M. Cao, D. Kelly, A. Schmid, D.T. Skelly,

A. Themistocleous, T. Dong, S. Field, E. Hamilton, E. Kelly, P. Klenerman, J.C. Knight, Y. Lie, C. Petropoulos, C. Sedik, T. Wrin, G. Meddaugh, Y. Peng, G. Screaton, E. Stafford, C.V.T.G. the Oxford, T cell and antibody responses induced by a single dose of ChAdOx1 nCoV-19 (AZD1222) vaccine in a phase 1/2 clinical trial, Nat. Med. 27 (2) (2021) 270–278.

[63] A.P.S. Munro, L. Janani, V. Cornelius, P.K. Aley, G. Babbage, D. Baxter, M. Bula, K. Cathie, K. Chatterjee, K. Dodd, Y. Enever, K. Gokani, A.L. Goodman, C.A. Green, L. Harndahl, J. Haughney, A. Hicks, A.A. van der Klaauw, J. Kwok, T. Lambe, V. Libri, M.J. Llewelyn, A.C. McGregor, A.M. Minassian, P. Moore, M. Mughal, Y.F. Mujadidi, J. Murira, O. Osanlou, R. Osanlou, D.R. Owens, M. Pacurar, A. Palfreeman, D. Pan, T. Rampling, K. Regan, S. Saich, J. Salkeld, D. Saralaya, S. Sharma, R. Sheridan, A. Sturdy, E.C. Thomson, S. Todd, C. Twelves, R.C. Read, S. Charlton, B. Hallis, M. Ramsay, N. Andrews, J.S. Nguyen-Van-Tam, M.D. Snape, X. Liu, S.N. Faust, A. Riordan, A. Ustianowski, C.A. Rogers, S. Hughes, L. Longshaw, J. Stockport, R. Hughes, L. Grundy, L. Tudor Jones, A. Egbe, E. Snashall, T. Eadsforth, S. Reeder, K. Storton, M. Munusamy, B. Tandy, A. Egbo, S. Cox, N.N. Ahmed, A. Shenoy, R. Bousfield, D. Wixted, H. Gutteridge, B. Mansfield, C. Herbert, K. Holliday, J. Calderwood, D. Barker, J. Brandon, L. Tulloch, S. Colquhoun, H. Thorp, H. Radford, J. Evans, H. Baker, J. Thorpe, S. Batham, J. Hailstone, R. Phillips, D. Kumar, F. Westwell, F. Makia, N. Hopkins, L. Barcella, M. Mpelembue, M. dabagh, M. lang, F. khan, O. Adebambo, S. Chita, T. Corrah, A. Whittington, L. John, S. Roche, L. Wagstaff, A. Farrier, K. Bisnauthsing, T. Serafimova, E. Nanino, E. Cooney, J. Wilson-Goldsmith, H. Nguyen, A. Mazzella, B. Jackson, S. Aslam, T. Bawa, S. Broadhead, S. Farooqi, J. Piper, R. Weighell, L. Pickup, D. Shamtally, J. Domingo, E. Kourampa, C. Hale, J. Gibney, M. Stackpoole, Z. Rashid–Gardner, R. Lyon, C. McDonnell, C. Cole, A. Stewart, G. McMillan, M. Savage, H. Beckett, C. Moorbey, A. Desai, C. Brown, K. Naker, E. Qureshi, C. Trinham, C. Sabine, S. Moore, S. Hurdover, E. Justice, D. Smith, E. Plested, C. Ferreira Da Silva, R. White, H. Robinson, L. Cifuentes, G. Morshead, R. Drake-Brockman, P. Kinch, M. Kasanyinga, E.A. Clutterbuck, S. Bibi, A.S.V. Stuart, R.H. Shaw, M. Singh, T. Champaneri, M. Irwin, M. Khan, A. Kownacka, M. Nabunjo, C. Osuji, J. Hladkiwskyj, D. Galvin, G. Patel, J. Mouland, B. Longhurst, M. Moon, B. Giddins, C. Pereira Dias Alves, L. Richmond, C. Minnis, S. Baryschpolec, S. Elliott, L. Fox, V. Graham, N. Baker, K. Godwin, K. Buttigieg, C. Knight, P. Brown, P. Lall, I. Shaik, E. Chiplin, E. Brunt, S. Leung, L. Allen, S. Thomas, S. Fraser, B. Choi, J. Gouriet, A. Freedman, J. Perkins, A. Gowland, J. Macdonald, J.P. Seenan, I. Starinskij, A. Seaton, E. Peters, S. Singh, B. Gardside, A. Bonnaud, C. Davies, E. Gordon, S. Keenan, J. Hall, S. Wilkins, S. Tasker, R. James, I. Seath, K. Littlewood, J. Newman, I. Boubriak, D. Suggitt, H. Haydock, S. Bennett, W. Woodyatt, K. Hughes, J. Bell, T. Coughlan, D. van Welsenes, M. Kamal, C. Cooper, S. Tunstall, N. Ronan, R. Cutts, T. Dare, Y.T.N. Yim, S. Whittley, M. Ricamara, S. Hamal, K. Adams, H. Baker, K. Driver, N. Turner, T. Rawlins, S. Roy, M. Merida-Morillas, Y. Sakagami, A. Andrews, L. Goncalves cordeiro, M. Stokes, W. Ambihapathy, J. Spencer, N. Parungao, L. Berry, J. Cullinane, L. Presland, A. Ross-Russell, S. Warren, J. Baker, A. Oliver, A. Buadi, K. Lee, L. Haskell, R. Romani, I. Bentley, T. Whitbred, S. Fowler, J. Gavin, A. Magee, T. Watson, K. Nightingale, P. Marius, E. Summerton, E. Locke, T. Honey, A. Lingwood, A. de la Haye, R.S. Elliott, K. Underwood, M. King, S. Davies-Dear, E. Horsfall, O. Chalwin, H. Burton, C.J. Edwards, B. Welham, S. Garrahy, F. Hall, E. Ladikou, D. Mullan, D. Hansen, M. Campbell, F. Dos Santos, H. Habash-Bailey, N. Lakeman, D. Branney, L. Vamplew, A. Hogan, J. Frankham, M. Wiselka, D. Vail, V. Wenn, V. Renals, K. Ellis, J. Lewis-Taylor, J. Magan, A. Hardy, K. Appleby, Safety and immunogenicity of seven COVID-19 vaccines as a third dose (booster) following two doses of ChAdOx1 nCov-19 or BNT162b2 in the UK (COV-BOOST): a blinded, multicentre, randomised, controlled, phase 2 trial, Lancet N. Am. Ed. 398 (10318) (2021) 2258–2276.

[64] Y. Liu, Q. Zeng, C. Deng, M. Li, L. Li, D. Liu, M. Liu, X. Ruan, J. Mei, R. Mo, Q. Zhou, M. Liu, S. Peng, J. Wang, H. Zhang, H. Xiao, Robust induction of B cell and T cell responses by a third dose of inactivated SARS-CoV-2 vaccine, Cell Discov. 8 (1) (2022) 10.

[65] N.D. Pennock, J.T. White, E.W. Cross, E.E. Cheney, B.A. Tamburini, R.M. Kedl, T cell responses: naive to memory and everything in between, Adv. Physiol. Educ. 37 (4) (2013) 273–283.

[66] K.W. Cohen, S.L. Linderman, Z. Moodie, J. Czartoski, L. Lai, G. Mantus, C. Norwood, L.E. Nyhoff, V.V. Edara, K. Floyd, S.C. De Rosa, H. Ahmed, R. Whaley, S.N. Patel, B. Prigmore, M.P. Lemos, C.W. Davis, S. Furth, J.B. O'Keefe, M.P. Gharpure, S. Gunisetty, K. Stephens, R. Antia, V.I. Zarnitsyna, D.S. Stephens, S. Edupuganti, N. Rouphael, E.J. Anderson, A.K. Mehta, J. Wrammert, M.S. Suthar, R. Ahmed, M.J. McElrath, Longitudinal analysis shows durable and broad immune memory after SARS-CoV-2 infection with persisting antibody responses and memory B and T cells, Cell Rep. Med. 2 (7) (2021) 100354 -100354.

[67] K.W. Cohen, S.L. Linderman, Z. Moodie, J. Czartoski, L. Lai, G. Mantus, C. Norwood, L.E. Nyhoff, V.V. Edara, K. Floyd, S.C. De Rosa, H. Ahmed, R. Whaley, S.N. Patel, B. Prigmore, M.P. Lemos, C.W. Davis, S. Furth, J. O'Keefe, M.P. Gharpure, S. Gunisetty, K.A. Stephens, R. Antia, V.I. Zarnitsyna, D.S. Stephens, S. Edupuganti, N. Rouphael, E.J. Anderson, A.K. Mehta, J. Wrammert, M.S. Suthar, R. Ahmed, M.J. McElrath, Longitudinal analysis shows durable and broad immune memory after SARS-CoV-2 infection with persisting antibody responses and memory B and T cells, medRxiv (2021).

[68] S. Yang, F. Liu, Q.J. Wang, S.A. Rosenberg, R.A. Morgan, The shedding of CD62L (L-selectin) regulates the acquisition of lytic activity in human tumor reactive T lymphocytes, PLoS One 6 (7) (2011) e22560 -e22560.

[69] F. Guirakhoo, L. Kuo, J. Peng, J.H. Huang, B.S. Kuo, F. Lin, Y.J. Liu, Z. Liu, G. Wu, S. Ding, K.L. Hou, J. Cheng, V. Yang, H. Jiang, J. Wang, T. Chen, W. Xia,

E. Lin, C.H. Hung, H.J. Chen, Z. Shih, Y.L. Lin, S. Wang, V. Ryan, B.T. Schurter, M.M. Hu, G. Heppner, D.C. Malherbe, A. Bukreyev, M. Hellerstein, T.P. Monath, C.Y. Wang, A Novel SARS-CoV-2 multitope protein/peptide vaccine candidate is highly immunogenic and prevents lung infection in an AAV hACE2 mouse model and non-human primates, bioRxiv (2021) 2020.11.30.399154.

[70] B. Ganneru, H. Jogdand, V.K. Daram, D. Das, N.R. Molugu, S.D. Prasad, S.V. Kannappa, K.M. Ella, R. Ravikrishnan, A. Awasthi, J. Jose, P. Rao, D. Kumar, R. Ella, P. Abraham, P.D. Yadav, G.N. Sapkal, A. Shete-Aich, G. Desphande, S. Mohandas, A. Basu, N. Gupta, K.M. Vadrevu, Th1 skewed immune response of whole virion inactivated SARS CoV 2 vaccine and its safety evaluation, iScience 24 (4) (2021) 102298.

[71] D.T. Skelly, A.C. Harding, J. Gilbert-Jaramillo, M.L. Knight, S. Longet, A. Brown, S. Adele, E. Adland, H. Brown, T. Tipton, L. Stafford, A.J. Mentzer, S.A. Johnson, A. Amini, O.C. Group, T.K. Tan, L. Schimanski, K.Y.A. Huang, P. Rijal, J. Frater, P. Goulder, C.P. Conlon, K. Jeffery, C. Dold, A.J. Pollard, A. Sigal, T. de Oliveira, A.R. Townsend, P. Klenerman, S.J. Dunachie, E. Barnes, M.W. Carroll, W.S. James, C.M.P.C. Group, Two doses of SARS-CoV-2 vaccination induce robust immune responses to emerging SARS-CoV-2 variants of concern, Nat. Commun. 12 (1) (2021) 5061 -5061.

[72] B.A. Woldemeskel, C.C. Garliss, J.N. Blankson, SARS-CoV-2 mRNA vaccines induce broad $CD4^+$ T cell responses that recognize SARS-CoV-2 variants and HCoV-NL63, J. Clin. Invest. 131 (10) (2021).

[73] H. Tamber, P. Johansen, H.P. Merkle, B. Gander, Formulation aspects of biodegradable polymeric microspheres for antigen delivery, Adv. Drug. Deliv. Rev. 57 (3) (2005) 357–376.

[74] E. Jafarifar, M. Hajialyani, M. Akbari, M. Rahimi, Y. Shokoohinia, A. Fattahi, Preparation of a reproducible long-acting formulation of risperidone-loaded PLGA microspheres using microfluidic method, Pharm. Dev. Technol. 22 (6) (2017) 836–843.

[75] N. Bock, M.A. Woodruff, D.W. Hutmacher, T.R. Dargaville, Electrospraying, a reproducible method for production of polymeric microspheres for biomedical applications, Polymers 3 (1) (2011) 131–149.

[76] C.K. Chen, P.K. Huang, W.C. Law, C.H. Chu, N.T. Chen, L.W. Lo, Biodegradable polymers for gene-delivery applications, Int. J. Nanomed. 15 (2020) 2131–2150.

[77] S.R. Jameela, N. Suma, A. Misra, R. Raghuvanshi, S. Ganga, A. Jayakrishnan, Poly(ε-caprolactone) microspheres as a vaccine carrier, Curr. Sci. 70 (7) (1996) 669–671.

[78] W. Kastenmüller, K. Kastenmüller, C. Kurts, R.A. Seder, Dendritic cell-targeted vaccines–hope or hype? Nat. Rev. Immunol. 14 (10) (2014) 705–711.

[79] R. Pearlman, T.A. Bewley, Stability and characterization of human growth hormone, in: Stability and Characterization of Protein and Peptide Drugs: Case Histories, Springer US, Boston, MA, 1993, pp. 1–58.

[80] E. Risson, Inactivated vaccine for SARS-CoV-2, Nat. Rev. Immunol. 20 (6) (2020) 353 -353.

[81] D. Gupta, H. Parthasarathy, V. Sah, D. Tandel, D. Vedagiri, S. Reddy, K.H. Harshan, Inactivation of SARS-CoV-2 by β-propiolactone causes aggregation of viral particles and loss of antigenic potential, Virus Res. 305 (2021) 198555 -198555.

[82] A. Sánchez, B. Villamayor, Y. Guo, J. McIver, M.a.J. Alonso, Formulation strategies for the stabilization of tetanus toxoid in poly(lactide-co-glycolide) microspheres, Int. J. Pharm. 185 (2) (1999) 255–266.

[83] M.C. Manning, D.K. Chou, B.M. Murphy, R.W. Payne, D.S. Katayama, Stability of protein pharmaceuticals: an update, Pharm. Res. 27 (4) (2010) 544–575.

[84] M. Morlock, H. Koll, G. Winter, T. Kissel, Microencapsulation of rh-erythropoietin, using biodegradable poly(d,l-lactide-co-glycolide): protein stability and the effects of stabilizing excipients, Eur. J. Pharm. Biopharm. 43 (1) (1997) 29–36.

[85] M. Morlock, T. Kissel, Y.X. Li, H. Koll, G. Winter, Erythropoietin loaded microspheres prepared from biodegradable LPLG–PEO–LPLG triblock copolymers: protein stabilization and in-vitro release properties, J. Control. Release 56 (1) (1998) 105–115.

[86] K.G. Carrasquillo, J.C.A. Carro, A. Alejandro, D.D. Toro, K. Griebenow, Reduction of structural perturbations in bovine serum albumin by non-aqueous microencapsulation, J. Pharm. Pharmacol. 53 (1) (2001) 115–120.

[87] R. Audran, Y. Men, P. Johansen, B. Gander, G. Corradin, Enhanced immunogenicity of microencapsulated tetanus toxoid with stabilizing agents, Pharm. Res. 15 (7) (1998) 1111–1116.

[88] P. Moss, The T cell immune response against SARS-CoV-2, Nat. Immunol. 23 (2) (2022) 186–193.

[89] K. Röltgen, A.E. Powell, O.F. Wirz, B.A. Stevens, C.A. Hogan, J. Najeeb, M. Hunter, H. Wang, M.K. Sahoo, C. Huang, F. Yamamoto, M. Manohar, J. Manalac, A.R. Otrelo-Cardoso, T.D. Pham, A. Rustagi, A.J. Rogers, N.H. Shah, C.A. Blish, J.R. Cochran, T.S. Jardetzky, J.L. Zehnder, T.T. Wang, B. Narasimhan, S. Gombar, R. Tibshirani, K.C. Nadeau, P.S. Kim, B.A. Pinsky, S.D. Boyd, Defining the features and duration of antibody responses to SARS-CoV-2 infection associated with disease severity and outcome, Sci. Immunol. 5 (54) (2020) eabe0240.

[90] Q.X. Long, B.Z. Liu, H.J. Deng, G.C. Wu, K. Deng, Y.K. Chen, P. Liao, J.F. Qiu, Y. Lin, X.F. Cai, D.Q. Wang, Y. Hu, J.H. Ren, N. Tang, Y.Y. Xu, L.H. Yu, Z. Mo, F. Gong, X.L. Zhang, W.G. Tian, L. Hu, X.X. Zhang, J.L. Xiang, H.X. Du, H.W. Liu, C.H. Lang, X.H. Luo, S.B. Wu, X.P. Cui, Z. Zhou, M.M. Zhu, J. Wang, C.J. Xue, X.F. Li, L. Wang, Z.J. Li, K. Wang, C.C. Niu, Q.J. Yang, X.J. Tang, Y. Zhang, X.M. Liu, J.J. Li, D.C. Zhang, F. Zhang, P. Liu, J. Yuan, Q. Li, J.L. Hu, J. Chen, A.L. Huang, Antibody responses to SARS-CoV-2 in patients with COVID-19, Nat. Med. 26 (6) (2020) 845–848.

[91] A.S. Iyer, F.K. Jones, A. Nodoushani, M. Kelly, M. Becker, D. Slater, R. Mills, E. Teng, M. Kamruzzaman, W.F. Garcia-Beltran, M. Astudillo, D. Yang, T.E. Miller, E. Oliver, S. Fischinger, C. Atyeo, A.J. Iafrate, S.B. Calderwood, S.A. Lauer, J. Yu, Z. Li, J. Feldman, B.M. Hauser, T.M. Caradonna, J.A. Branda, S.E. Turbett, R.C. LaRocque, G. Mellon, D.H. Barouch, A.G. Schmidt, A.S. Azman, G. Alter, E.T. Ryan, J.B. Harris, R.C. Charles, Persistence and decay of human antibody responses to the receptor binding domain of SARS-CoV-2 spike protein in COVID-19 patients, Sci. Immunol. 5 (52) (2020).

[92] R. Rose, F. Neumann, O. Grobe, T. Lorentz, H. Fickenscher, A. Krumbholz, Humoral immune response after different SARS-CoV-2 vaccination regimens, BMC Med. 20 (1) (2022) 31.

[93] L. Esparcia-Pinedo, P. Martínez-Fleta, N. Ropero, P. Vera-Tomé, H.T. Reyburn, J.M. Casasnovas, J.M. Rodríguez Frade, M. Valés-Gómez, C. Vilches, E. Martín–Gayo, C. Muñoz-Calleja, F. Sanchez-Madrid, A. Alfranca, CD^{4+} T cell immune specificity changes after vaccination in healthy and COVID-19 convalescent subjects, Front. Immunol. 12 (2022).

[94] R.R. Goel, M.M. Painter, S.A. Apostolidis, D. Mathew, W. Meng, A.M. Rosenfeld, K.A. Lundgreen, A. Reynaldi, D.S. Khoury, A. Pattekar, S. Gouma, L. Kuri-Cervantes, P. Hicks, S. Dysinger, A. Hicks, H. Sharma, S. Herring, S. Korte, A.E. Baxter, D.A. Oldridge, J.R. Giles, M.E. Weirick, C.M. McAllister, M. Awofolaju, N. Tanenbaum, E.M. Drapeau, J. Dougherty, S. Long, K. D'Andrea, J.T. Hamilton, M. McLaughlin, J.C. Williams, S. Adamski, O. Kuthuru, I. Frank, M.R. Betts, L.A. Vella, A. Grifoni, D. Weiskopf, A. Sette, S.E. Hensley, M.P. Davenport, P. Bates, E.T. Luning Prak, A.R. Greenplate, E.J. Wherry, mRNA vaccines induce durable immune memory to SARS-CoV-2 and variants of concern, Science 374 (6572) (2021) abm0829.

[95] H. Parry, R. Bruton, G. Tut, M. Ali, C. Stephens, D. Greenwood, S. Faustini, S. Hughes, A. Huissoon, R. Meade, K. Brown, G. Amirthalingam, A. Otter, B. Hallis, A. Richter, J. Zuo, P. Moss, Immunogenicity of single vaccination with BNT162b2 or ChAdOx1 nCoV-19 at 5-6 weeks post vaccine in participants aged 80 years or older: an exploratory analysis, Lancet Healthy Longev 2 (9) (2021) e554–e560.

[96] H. Parry, R. Bruton, C. Stephens, K. Brown, G. Amirthalingam, A. Otter, B. Hallis, J. Zuo, P. Moss, Differential immunogenicity of BNT162b2 or ChAdOx1 vaccines after extended-interval homologous dual vaccination in older people, Immun. Ageing 18 (1) (2021) 34.

[97] A.S.V. Stuart, R.H. Shaw, X. Liu, M. Greenland, P.K. Aley, N.J. Andrews, J.C. Cameron, S. Charlton, E.A. Clutterbuck, A.M. Collins, T. Darton, T. Dinesh, C.J.A. Duncan, A. England, S.N. Faust, D.M. Ferreira, A. Finn, A.L. Goodman, C.A. Green, B. Hallis, P.T. Heath, H. Hill, B.M. Horsington, T. Lambe, R. Lazarus, V. Libri, P.J. Lillie, Y.F. Mujadidi, R. Payne, E.L. Plested, S. Provstgaard-Morys, M.N. Ramasamy, M. Ramsay, R.C. Read, H. Robinson, G.R. Screaton, N. Singh, D.P.J. Turner, P.J. Turner, I. Vichos, R. White, J.S. Nguyen-Van-Tam, M.D. Snape, Immunogenicity, safety, and reactogenicity of heterologous COVID-19 primary vaccination incorporating mRNA, viral-vector, and protein-adjuvant vaccines in the UK (Com-COV2): a single-blind, randomised, phase 2, non-inferiority trial, Lancet N. Am. Ed. 399 (10319) (2022) 36–49.

[98] R.H. Shaw, A. Stuart, M. Greenland, X. Liu, J.S. Nguyen Van-Tam, M.D. Snape, Heterologous prime-boost COVID-19 vaccination: initial reactogenicity data, Lancet 397 (10289) (2021) 2043–2046.

[99] J.S. Heitmann, T. Bilich, C. Tandler, A. Nelde, Y. Maringer, M. Marconato, J. Reusch, S. Jäger, M. Denk, M. Richter, L. Anton, L.M. Weber, M. Roerden, J. Bauer, J. Rieth, M. Wacker, S. Hörber, A. Peter, C. Meisner, I. Fischer, M.W. Löffler, J. Karbach, E. Jäger, R. Klein, H.G. Rammensee, H.R. Salih, J.S. Walz, A COVID-19 peptide vaccine for the induction of SARS-CoV-2 T cell immunity, Nature 601 (7894) (2022) 617–622.

[100] W. Jiang, R.K. Gupta, M.C. Deshpande, S.P. Schwendeman, Biodegradable poly(lactic-co-glycolic acid) microparticles for injectable delivery of vaccine antigens, Adv. Drug. Deliv. Rev. 57 (3) (2005) 391–410.

[101] U.S.F.D. ADMINISTRATION, COVID-19 vaccines, 2022. https://www.fda.gov/emergency-preparedness-and-response/coronavirus-disease-2019-covid-19/covid-19-vaccines#authorized-vaccines.

[102] H. Huatan, J.H. Collett, D. Attwood, C. Booth, Preparation and characterization of poly(ε-caprolactone) polymer blends for the delivery of proteins, Biomaterials 16 (17) (1995) 1297–1303.

[103] E.R. Balmayor, K. Tuzlakoglu, H.S. Azevedo, R.L. Reis, Preparation and characterization of starch-poly-ε-caprolactone microparticles incorporating bioactive agents for drug delivery and tissue engineering applications, Acta Biomater. 5 (4) (2009) 1035–1045.

[104] H.B. Ravivarapu, K. Burton, P.P. DeLuca, Polymer and microsphere blending to alter the release of a peptide from PLGA microspheres, Eur. J. Pharm. Biopharm. 50 (2) (2000) 263–270.

[105] K.G.H. Desai, S.P. Schwendeman, Active self-healing encapsulation of vaccine antigens in PLGA microspheres, J. Control. Release 165 (1) (2013) 62–74 official journal of the Controlled Release Society.